VALIDATION OF A PERSONALIZED PEDIATRIC 3D-PRINTED PHANTOM FOR OUT-OF-FIELD PHOTON AND PROTON DOSIMETRY

By

Amanda E. Swanson

A THESIS

Presented to the Medical Physics Graduate Program
and the Oregon Health & Science University
School of Medicine

in partial fulfillment of
the requirements for the degree of

Master of Science

June 2020

School of Medicine

Oregon Health & Science University

CERTIFICATE OF APPROVAL

This is to certify that the Master's Thesis of

Amanda E. Swanson

has been approved

Mentor/Advisor – Dr. Kyle Gallagher

Member – Dr. Phillip Taddei

Member – Monica Kishore

Member – Dr. Richard Crilly

Table of Contents

Table of Figures

Table of Tables

List of Abbreviations

SMN: Secondary malignant neoplasm

DNA: deoxyribonucleic acid

3D: Three dimensional

MV: Megavolts

MeV: Megaelectron volts

PLA: polylactic acid

PVC: polyvinyl chloride

D: Absorbed dose

D_{Rx}: Prescription dose

H: Equivalent dose

RBE: Relative Biological Effectiveness

Acknowledgements

Thank you to the collaborators on this project: to Phillip Taddei and Dominic Maes at University of Washington, and Wayne Newhauser at Louisiana State University for establishing the foundation of this project and assisting with the direction of its continuation; to Paola Alvarez at IROC Houston for advising on the setup and analysis of TLDs used in this study; to Tiffany Ashley at Oregon Health & Science University (OHSU) for helping set up immobilization for the 3D-printed phantom; and to Hunter Tillery, Margaret Carey, and Meagan Moore for all of the work you put in that made this study possible.

Thank you to the Association for Medical Physics Students at OHSU. I enjoyed creating a community while we were here, and I look forward to seeing you all throughout our careers.

Thank you to my advisors, Kyle Gallagher and Monica Kishore. Your enthusiasm and feedback have been instrumental not only to the project, but to deciding the direction of my career in Medical Physics. I am so grateful to have learned from you this past year.

Thank you to everyone in OHSU's Radiation Medicine department for making me feel welcome. I am lucky to have learned from and worked with all of you.

Finally - thank you, as always, to Ajit.

Abstract

Purpose: The purpose of this study was to first validate a 3D-printed personalized pediatric phantom for use in out-of-field photon and proton dosimetry, and to secondarily assess the impact of phantom design on the accuracy of out-of-field dose measurements.

Methods: A customized 3D-printed phantom was constructed at Louisiana State University to approximate a commercial anthropomorphic phantom (ATOM 10-year-old Model 706, CIRS, Inc., Norfolk, Virginia). The commercial phantom simulates a 10-year-old female and incorporates tissue heterogeneities, whereas the 3D-printed phantom has an identical exterior contour filled with water to approximate tissue. A third phantom approximating the commercial phantom was constructed using solid water blocks. In these three phantoms, a Varian TrueBeam (Varian Medical Systems, Palo Alto, CA) was used to deliver a 6 megavoltage intracranial photon field (10 x 10 cm^2) at Oregon Health & Science University. Absorbed dose was measured using thermoluminescent dosimeters (TLD-100, Imaging and Radiation Oncology Core, Houston, Texas) at four radiosensitive locations: thyroid, esophagus, small bowel, and gonads. The TLD-100s were processed by MD Anderson's Imaging and Radiation Oncology Core Quality Assurance Center. A sensitivity test of the dosimeter placement was conducted using an ionization chamber (Type 30013, PTW-Freiburg, Freiburg, Germany). Out-of-field absorbed dose measurements for a cranial pencil-beam scanning proton field were taken at the Seattle Cancer Care Alliance Proton Therapy Center at the thyroid, esophagus, and gonads using an ion chamber filled with tissue-equivalent gas (Wellhoffer IC-30, Ion Beam Applications, Louvain-La-Neuve, Belgium). Measurements for proton therapy were compared to absorbed doses

calculated using a clinical treatment planning system supplemented with a secondary neutron analytical model from the literature.

Results: For photon therapy, the out-of-field absorbed dose per prescription dose (D/D_{Rx}) at each location varied by less than 17.4% (0.146 cGy/Gy) between the 3D-printed, solid water, and anthropomorphic phantoms. The largest variation was observed between the solid water and 3D-printed phantoms at the thyroid, which was close to the field edge. Compared to the commercial phantom, the solid water and 3D-printed phantoms overestimated D/D_{Rx} by approximately 11% (0.031 cGy/Gy and 0.028 cGy/Gy, respectively) at the esophagus, which is near lung tissue. At the gonads, the variation was less than 7.7% (0.002 cGy/Gy) across all three phantoms. The sensitivity test resulted in up to a 15.2% and 60.6% change in out-of-field dose from a 1.0 and 3.0 cm displacement of the dosimeter, respectively. For proton therapy, D/D_{Rx} was considerably lower than photon therapy at each measurement location, and the gonad measurement was indistinguishable from background. Measured D/D_{Rx} for proton therapy was 44% lower than the calculated D/D_{Rx} at the thyroid (4.85 mGy/Gy), but beyond 10 cm from the field edge where the dose was of non-clinical significance the agreement diverged such that the measured D/D_{Rx} was a factor of 8 larger than the calculated D/D_{Rx} at the esophagus (0.123 mGy/Gy).

Conclusions: This study presented a preliminary validation for the use of a personalized 3D-printed phantom for out-of-field photon dosimetry and provided an initial test for use in out-of-field proton dosimetry. This work also demonstrated that accuracy in dosimeter placement with respect to the field edge was of equal or greater importance than phantom design when measuring out-of-field dose for photon therapy.

1. Introduction

Advances in radiation therapy have resulted in dramatically increased lifespans for patients undergoing treatment, particularly those in the pediatric population. Improved treatment techniques for external beam radiation therapy have contributed significantly to increasing survival rates of these patients (Newhauser & Durante, 2011; Salloum et al., 2019; Stokkevag et al., 2017; Smith et al., 2010): cancer statistics reported that the 5-year survival rates for pediatric cancer patients increased from 58% to 83% from the 1970s to 2014 (Siegel et al., 2019). However, late effects from treatment can appear decades after irradiation, and as survival times for patients increase the onset of secondary complications and late radiation effects become more apparent (Armstrong et al., 2010; Newhauser et al., 2016). A report from the Childhood Cancer Survivorship Study found that pediatric medulloblastoma survivors treated with radiotherapy in the 1990s had a significantly higher 15-year cumulative secondary malignant neoplasm (SMN) incidence than those treated two decades prior, and were more likely to develop other severe health conditions (Salloum et al., 2019).

Pediatric patients are at an exceptionally high risk for developing secondary complications; the body's rapid development during childhood makes it more vulnerable to radiation damage, the small size positions radiosensitive organs closer to the primary field than for adults, and the drastically improved survival times for these patients increase the likelihood that radiation-induced complications will appear during their lives (Armstrong et al., 2010; Oeffinger et al., 2006; Berrington de Gonzalez et al., 2017). This risk can be mitigated in several ways, including referring pediatric cases to proton therapy centers (Taddei et al., 2018; Athar & Paganetti, 2011) and choosing highly conformal treatment methods such as image guided radiation therapy with

reduced margins surrounding the planning treatment volume (Newhauser et al., 2016). While care is taken to ensure that normal tissues are spared during treatment, dose to tissues outside of the primary treatment area – or "out-of-field" dose – is often not considered during treatment planning (Kry et al., 2017).

Out-of-field dose is defined as absorbed dose below the 50% prescription isodose curve and is commonly stratified as low ($\leq$ 5%) or intermediate (5-50%). While out-of-field doses are typically small compared to the prescribed dose, the risks associated with it vary depending on the treatment technique, energy, radiation quality, and the irradiated tissue (Kry et al., 2017; Newhauser et al., 2016). Studies have demonstrated that many secondary complications following radiation therapy treatments can be attributed to out-of-field dose making it critical to accurately quantify, characterize, and minimize out-of-field doses (Diallo et al., 2009).

While the composition of out-of-field doses are well understood across different modalities, they are difficult to quantify in clinical practice. One major challenge is the absence of anatomical information outside of the primary field, which both treatment planning systems and Monte Carlo methods rely on. This is because simulation computed tomography image sets have a limited field of view that allows for planning and dose calculation in the treatment planning system; whole-body images are not required, nor practical for this purpose. Previous work has focused on crafting methods to work around this limitation, including the development of supplemental computational phantoms (Gallagher et al., 2018; Howell et al., 2019; Gupta et al., 2020); however, even with complete anatomical information, treatment planning systems are unreliable for out-of-field dose evaluation. Photon treatment planning systems are not optimized to calculate dose outside of the primary field (Shine et al., 2019; Howell et al., 2010), and proton treatment planning systems do not account for neutron contributions to out-of-field dose. While the accuracy of Monte Carlo methods provides a useful

resource in specific cases, they are computationally expensive. Promising analytical models have been developed that offer expedient out-of-field dose estimation (Newhauser et al., 2017), including those for photon (Taddei et al., 2013; Schneider et al., 2019; Wilson et al., 2020) and proton therapies (Gallagher & Taddei, 2018; Hälg & Schneider, 2020; Eley et al., 2015; Newhauser et al., 2017). To validate these calculation methods, direct measurements in phantoms are considered the "gold standard" for quantifying out-of-field dose.

Phantoms are used as surrogates for patients because in-vivo organ dose measurements are not feasible for patients undergoing treatment. These phantoms range from very simple to highly sophisticated. Solid water blocks are inexpensive and widely available in most clinical settings, but their rigid forms and uniform densities limit the extent to which they can emulate the shape and tissue variation of a human patient. Highly detailed commercial phantoms can replicate these features, but they have significant limitations. Commercial phantoms only represent a limited set of generalized human models and cannot be modified to reflect an individual's anatomy. Additionally, the high costs of a whole-body commercial phantoms make them inaccessible to most clinics. These limitations make the production of customizable, relatively inexpensive phantoms a desirable alternative for out-of-field dose measurement.

Three dimensional (3D) printed phantoms offer a potential solution to this problem, and there has been increasing interest in using 3D-printing for various roles within radiation oncology (Rooney et al., 2020). Prior work has demonstrated the feasibility of using a full-body 3D-printed water-filled phantom of Louisiana State University's design to characterize out-of-field dose measurements in photon, proton, and neutron therapies (Tillery, 2019). Previous studies have also explored different 3D-printing designs for use in radiotherapy, including a full-scale, patient-specific torso phantom that uses the absence of infill to represent air cavities (Craft & Howell, 2017). 3D-printing fabrication methods have been evaluated by assessing the

uncertainties of 3D-printing technology (Craft et al., 2018) and the accuracy of contour reproduction using light-field scans (Carey, 2019). This method can be personalized and produced at relatively little cost and may enable clinics to directly evaluate out-of-field doses for high-risk patients. However, the validation of using a 3D-printed phantom for clinical out-of-field photon and proton dosimetry is lacking in the literature. Furthermore, while a highly detailed phantom seems ideal for accurate measurements of out-of-field dose, there is a need to explicitly compare out-of-field dose measurements between a "plastic slab" phantom and anthropomorphic phantoms (Kry et al., 2017). This is in part due to the unique characteristics of out-of-field dose, which may not require the same level of anthropomorphic detail in phantom design as in-field dose determination.

The purpose of this study was to validate the use of a 3D-printed pediatric phantom for out-of-field dose measurements in photon and proton therapy treatments, and to evaluate the impact of phantom design on the accuracy of out-of-field dose measurements for photon therapy. For this study, a 3D-printed phantom prototype was designed and constructed at Louisiana State University to emulate an existing commercial anthropomorphic phantom (ATOM 10-year-old Model 706, CIRS, Inc., Norfolk, Virginia). This prototype uses light-field scans to design and print a lightweight polylactic (PLA) shell to match the exterior contour of an existing model or patient, which is then filled with water during measurement (Carey, 2019). Out-of-field photon doses taken in the 3D-printed phantom were evaluated by measuring out-of-field dose in the 3D-printed phantom, the commercial phantom it emulates, and a solid water phantom and comparing the absorbed dose per prescription dose (D/D_{Rx}) in cGy/Gy. Out-of-field proton dosimetry was evaluated in the 3D-printed phantom by comparing D/D_{Rx} measurements to calculated values generated using RayStation (RaySearch Medical Laboratories AB, Stockholm, Sweden) and an analytical model from the literature (Gallagher & Taddei, 2018).

2. Background

2.1. Secondary complications

Radiation interactions in tissue can result in two types of damage: deterministic, or non-stochastic, in which damaged cells are destroyed by incident radiation; and stochastic, where radiation damages the cell's deoxyribonucleic acid (DNA) without killing the host cell (Hall & Amato, 2019). These cells have the potential to replicate without fixing the damaged DNA and initiate secondary effects, such as carcinogenesis. For deterministic effects there is a threshold dose below which effects do not manifest, but above this threshold the severity increases with administered dose. However, while the probability of stochastic effects increases with dose, the severity of these effects is independent of the magnitude of the dose (NCRP, 1993).

A commonly known complication is the development of SMN, which are thought to occur as a result of unrepaired chromosome aberrations caused by radiation exposure. Much of the evidence of radiation-induced cancer comes stems from the Life Span Study cohort of the atomic bomb survivors' database, the most comprehensive database concerning effects of radiation on the human body over time. Reports from this study were instrumental in constructing our current understanding of radiation damage in tissue, including the induction of deterministic and stochastic effects. However, there are several limitations to the study including the variance in the effects between high dose and high dose rate of the exposures. This study demonstrated a linear relationship between dose and increased radiation carcinogenesis for high doses but found insufficient epidemiological data to determine the relationship at doses below 50 mSv. Below 50 mSv, the dose response relationship for carcinogenesis is unknown (Brenner et al., 2003). However, the theory most widely adopted by regulatory and medical associations for dose response in this region is the "linear no-threshold"

model in which the linear response is extrapolated to the low dose region, with no dose threshold for stochastic effects (National Research Council, 2006).

2.2. Risk factors

Longitudinal studies with long-term outcomes of cancer patients that report the rate of excess SMN development for patients following radiation therapy support the presence of increased risk for patients undergoing radiation therapy (Armstrong et al., 2010; Diallo et al., 2009). While the studies are complicated by the study cohorts themselves, since patients requiring radiation therapy may already be at a higher risk of developing a second health condition, they have further identified important risk factors and shaped improvements in treatment. One such risk factor is the distribution and quantity of out-of-field dose. Research studies have observed excess SMNs at locations outside of the primary treatment field in patients following radiation therapy, suggesting that doses outside of the primary treatment site can significantly increase a patient's risk (Diallo et al., 2009; Newhauser et al., 2016; Stokkevag et al., 2017; Brenner et al., 2000).

Risk of SMN development has the potential to be accounted for in treatment planning by minimizing doses to normal (non-cancerous) tissues. Currently, doses in normal tissues within the treatment field are constrained during tSreatment planning to minimize the risk of acute toxicities, but SMN risk is not typically considered. Many treatment techniques can minimize dose to normal tissues outside of the treatment field including carefully orienting beams with respect to the patient, minimizing photon beam modulation, or applying pencil-beam scanning particle therapy as an alternative to passively-scattered beams and photon therapy (Athar & Paganetti, 2011; Kaderka et al., 2012; Newhauser et al., 2009).

Many factors affect the risk of developing SMN. Treatment location influences the distribution of dose to organs at risk (OAR) in the body: different organs have been shown to be more biologically responsive to radiation than others or have particularly detrimental effects on the patient's wellbeing when damaged, so care is taken to avoid dose to these OARs (ICRP, 2007). The patient's condition, genetics, and medical history also influences their risk of secondary complications (Newhauser & Durante, 2011). For example, patients taking medications that inhibit or modify immune responses may be more likely to develop a SMN following radiation therapy than others.

The risk of SMN development is particularly concerning for pediatric patients, for several key reasons. The first is that their rapidly developing tissues are more susceptible to the effects of radiation than adults: clinical guidelines estimate that pediatric patients are approximately ten times more radiosensitive to radiation effects than adults (National Research Council, 2006). The second reason is that the increased life expectancy for treated pediatric patients is longer than that of adults, so complications are more likely to arise during their lifetimes. The third reason is that pediatric patients simply have smaller bodies than adult patients; this indicates that the surrounding normal tissues are comparatively closer to the treatment site, which increases the out-of-field dose incident on these tissues. These risk factors for pediatric patients have resulted in long-term studies that evaluate outcomes for patients that had childhood photon treatments over several decades, such as the Childhood Cancer Survivorship Study (Armstrong et al., 2010; Oeffinger et al., 2006; Salloum et al., 2019). However, there is still a need to further evaluate long term effects in this patient population, particularly for those receiving proton therapy treatments (Berrington de Gonzalez et al., 2017).

2.3. Radiation therapy

Radiation therapy applies high-energy radiation to destroy unwanted lesions within the body (such as tumors) while sparing normal tissues as much as possible. This is accomplished by selecting the appropriate energy, radiation type, and treatment parameters to achieve the best radiation distribution in tissue and block undesired radiation from reaching OARs. Radiation therapy can be delivered internally through brachytherapy or nuclear medicine, or externally via external beam radiotherapy.

External beam radiotherapy can harness high-energy nuclear emissions from radioactive sources, such as Co-60 gamma emissions, or produce therapeutic radiation via the acceleration of charged particles. While the charged particles themselves – primarily electrons and protons – are sometimes applied directly, the most common form of external beam radiotherapy is administered via photon therapy.

2.3.1. Photon therapy

Photon therapy is advantageous because it has been extensively studied, and it is the most common form of radiation therapy delivery available today. Photon therapy is primarily administered via linear accelerators, or “linacs”. Figure 1 shows a simplified schematic of a typical linear accelerator. These linear accelerators produce photons by accelerating electrons to megaelectron volt energies (depending on the treatment needs and accelerator design) and directing them to collide with a tungsten alloy target to produce bremsstrahlung photons (Khan & Gibbons, 2014). This production method results in forward-peaked photons, which are delivered to the patient as a spectrum of photon energies with a maximum equal to the generated electron energy and an average energy approximately one third of the maximum

(Khan & Gibbons, 2014). Photon beams are therefore often characterized by the maximum energy of the spectrum in megavolts (MV). Flattening filters and collimation devices are used to modify the photon beam for patient treatments.

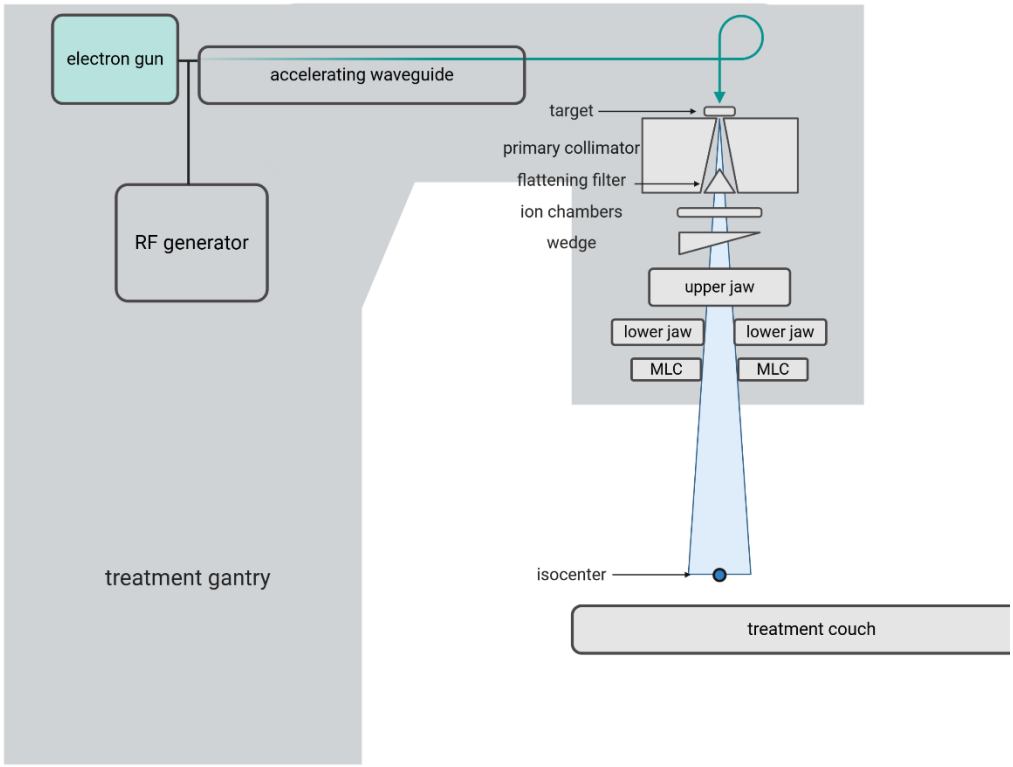

Figure 1: Simplified schematic of a commercial linear accelerator used for photon therapy treatment. Image features the gantry and head, treatment isocenter, and treatment couch. Electrons are represented by teal lines, and the photon beam is represented by a blue cone.

This form of radiation therapy is effective because of how high-energy photons interact with tissue. Absorbed dose from photon exposure is the amount of energy that is imparted from the ionizing radiation in atoms in matter, which occurs via specific interactions. High energy photons are indirectly ionizing in tissue, where the photon interacts with atomic particles to generate free radicals that can locally damage DNA and initiate cell death. The three most common

photon interactions in tissue are the photoelectric effect, Compton effect, and pair production (Khan & Gibbons, 2014). The probabilities of these interactions depend on energy of the photons, electron density of the material, and the atomic number of the medium.

Compton scattering is the primary photon interaction with tissue for photon therapy using a linear accelerator. In Compton scattering, photons transfer part of their initial energy to valence electrons in matter. This process results in a scattered photon and a fast electron: the fast electron deposits dose to nearby atoms via coulombic interactions, and the scattered photon may interact further to generate more fast electrons. This process is therefore highly dependent on the electron density, so the electron density is the most important property of the tissue when determining the probability of therapeutic-energy photon interactions. In this energy region, the probability of Compton scattering decreases with increasing photon energy (Khan & Gibbons, 2014).

In radiation therapy the energy of a photon beam is often characterized by a percent depth dose curve, where the percentage of absorbed dose is characterized as a function of depth in material. The percent depth dose curve highlights the skin sparing effect of photons: a 6 MV photon beam does not deposit its maximum dose in tissue until approximately 1.5 cm, and the dose to skin is comparatively low (Khan & Gibbons, 2014). Higher energy photons are more penetrating than lower energies, with a deeper level of 100% dose and a slower dose falloff with increasing depth.

While photons effectively spare skin dose to the patient, the absorbed dose peak is relatively shallow compared to the depth of most lesions, and the dose falloff is slow compared to charged particle therapies; treatment using external beam photon therapy always has some exit dose (beyond the depth of the target) and typically uses multiple beams entering at different

angles to focus absorbed dose at the target depth. X-rays of 6 MV are most often used for intracranial treatments, though higher energies are applied to minimize the maximum dose to normal tissues for larger anatomical sites such as the pelvis. However, for most treatments energies below 10 MV are preferred to minimize the production of neutrons in the treatment head.

2.3.2. Proton therapy

Proton therapy uses accelerated protons generated in linear accelerators, cyclotrons, or synchrocyclotrons to target lesions in the body (Wilson, 1946; Khan & Gibbons, 2014). Charged particles, such as protons, are ionizing radiation capable of disrupting DNA in tissue directly. Protons primarily interact with tissue via coulombic interactions with atomic electrons and nuclei, nuclear reactions, and bremsstrahlung (Newhauser & Zhang, 2015). The energy loss of charged particles in a medium is characterized by the "stopping power", which varies most strongly with material density for interactions in tissue (ICRU, 1993; Newhauser & Zhang, 2015). Consequently, atomic number is the dominant factor in tissue when considering proton therapy treatments.

Proton interactions with tissue are also characterized by the relationship with dose and depth: the energy a fast proton loses via coulombic and physical interactions in media is inversely proportional to the square of its velocity (Bethe, 1930; Bloch, 1933; Newhauser & Zhang, 2015). Therefore, the amount of energy a slowing proton can impart on surrounding atoms increases until it stops. This resulting peak in imparted energy at the proton's maximum penetration depth is dependent on the incident proton's energy and is referred to as the "Bragg peak" (Khan & Gibbons, 2014). The Bragg peak permits external beam radiotherapy treatments that have a

maximum dose at the depth of the lesion and no dose from the primary beam exiting the other side of the body. This dose deposition makes proton therapy a preferred modality for many kinds of treatment, such as craniospinal irradiation. Craniospinal proton irradiation is often applied for cancers of the central nervous system for pediatric patients. The lower integral dose and sharp falloff beyond the Bragg peak minimizes unnecessary exposure and significantly reduces dose to organs anterior to the targeted spine.

Despite the advantages of proton therapy, this modality is not as widely used as photon therapy for most clinical cases. Some of the reasons are economical – proton therapy units are currently far more expensive to build and are less widely available – but there are also some cases for which photon therapy is preferred. For example, patients with electronic implants, such as pacemakers, have a higher risk of device malfunction from proton therapy than photon therapy below 10 MV (Miften et al., 2019). This is because despite the highly localized dose delivered by the primary beam the composition of out-of-field dose is neutron-rich, and therefore has the potential to be highly disruptive to a life-preserving implanted device.

2.4. Out-of-field dose

2.4.1. Definitions and properties

Out-of-field dose – otherwise known as “stray” or “peripheral” radiation (Newhauser et al., 2017; Kaderka et al., 2012) – is defined as any absorbed dose to the patient outside of the primary treatment field, or absorbed dose below the 50% isodose surface (Kry et al., 2017). This isodose surface is defined as a percentage of the prescribed dose (D_{Rx}). It is further stratified as intermediate (5-50% D_{Rx}) and low dose (< 5% D_{Rx}). While these doses are considered small in comparison to the prescription dose, they are still large enough to warrant serious

consideration; multiple studies have shown that the development of secondary complications following radiation therapy originate outside of the primary field, and are thought to be the result of out-of-field dose (Diallo et al., 2009; Athar & Paganetti, 2011; Berrington de Gonzalez et al., 2013; Taddei et al., 2018).

The quantity and composition of out-of-field dose is dependent on many factors, including radiation quality, treatment modality, treatment technique, and design of the treatment head. The shielding and design of the treatment head significantly affect how the ionizing radiation scatters within the unit, thereby impacting the distribution of out-of-field dose resulting from these interactions. Treatment technique is a key factor in influencing out-of-field dose.

2.4.2. Photon considerations

Out-of-field dose from photon therapy below 10 MV has three major components: internal scatter, collimator scatter, and head leakage (Kry et al., 2017). Internal scatter is the result of photons from the primary treatment field scattering in tissue and depositing dose elsewhere in the body. Since these photons scatter within the patient, they are the dominant source of out-of-field dose near the field edge. Collimator scatter is due to photons colliding with the tungsten alloy collimation in the treatment head and scattering into the patient. Finally, head leakage is the result of photons scattering within the treatment head and escaping the shielding built into the unit. This is the primary contributor to out-of-field dose at distances further than approximately 20 cm from the central axis (Kase et al., 1983; Kry et al., 2017). Photon beams exceeding 10 MV also produce neutrons through photonuclear interactions with high-density collimating devices in the treatment head, which can contribute to out-of-field dose (Kry et al.,

2017; Zanini et al., 2004). Since cranial irradiation uses a 6 MV photon beam, this neutron dose is not a consideration for measurements.

Photon out-of-field dose exponentially decreases with increased distance from the field edge, particularly in intermediate-dose regions. Dose from internal scatter decreases rapidly with distance because of the larger amount of tissue traversed at large distances (i.e. attenuating material), and collimator scatter decreases with distance from the field edge because photons are less likely to be scattered at large angles from the collimator than small angles: high-energy therapeutic photons are forward-peaked, so they have a lower probability of scattering at the large angles required to contribute to out-of-field dose far from the field edge. However, as head leakage radiation dominates the dose falloff becomes shallower. This is in part due to the inverse-square law.

As distance from the field edge increases, the spectrum of photons slightly changes. Much of this is caused by scatter: as photons travel through attenuating material – such as shielding or large thicknesses of tissue – they are more likely to interact and scatter part of their energy via photons with lower energies outside of the primary field than they would be without travelling though attenuating material. This results in a “softer” spectrum of photon energies outside the primary field (Scarboro et al., 2011; Kry et al., 2017). Research has shown that depth beyond the depth of maximum absorption is not likely to be an important factor in out-of-field dose absorption (Kry et al., 2017).

Finally, highly conformal photon treatment methods such as intensity modulated radiation therapy (IMRT) or volumetric modulated arc therapy (VMAT) significantly affect the quantity of out-of-field dose for treatments. These methods modulate the intensity of the beam using multileaf collimators to increase treatment conformality and spare dose to nearby normal

tissues. However, this process requires an increase of monitor units (a measure of radiation output generated by the linear accelerator) by a factor of two or more (Hall & Wuu, 2003). This additional radiation generated in the treatment head increase the amount of collimator scatter and head leakage and contributes to more out-of-field dose.

2.4.3. Proton considerations

Out-of-field proton dose differs significantly from photon dose in some key ways, including the decreased integral dose and the strong presence of neutrons. Charged particle nuclear interactions with matter in both the treatment nozzle and within the patient generate secondary particles that can contribute to out-of-field radiation including neutrons, secondary protons, light charged particles, recoil heavy ions, and photons; among these, neutrons make up the vast majority of the dose equivalent (Kry et al., 2017; Hälg & Schneider, 2020). Protons and charged particles can contribute to out-of-field dose but are limited to areas close to the target volume, so out-of-field dose investigations for proton therapy are primarily concerned with neutrons (Hälg & Schneider, 2020).

Neutrons originating in the treatment head are “external”, whereas those originating from inside the patient are called “internal” neutrons. Out-of-field dose from both internal and external neutrons decreases as distance from the field edge increases (Zheng et al., 2007).

Passively scattered proton beams contribute a larger amount of out-of-field radiation originating from the treatment head than intensity-modulated “pencil-beam” scanning systems. This is because in passive scattering, scattering materials are placed in the path of the proton beam to spread the beam out, and the wide beam is incident on multiple layers of collimation – including field size collimation, apertures, and compensators – providing greater opportunities for nuclear

interactions in the treatment nozzle. Because of these interactions, approximately 85% of out-of-field dose from passive scattering proton therapy is composed of external neutrons (Newhauser et al., 2005; Kry et al., 2017; Zacharatou Jarlskog & Paganetti, 2008). Pencil beam scanning instead directs the proton beam into a small "pencil" beam using magnetic fields which is steered to deposit dose throughout the tumor volume (Lomax et al., 2001; Newhauser & Zhang, 2015). This method bypasses much of the collimation used in passive scattering, greatly reducing the external neutron contribution. Instead, internal neutrons make up the largest portion of out-of-field dose from scanning proton beams. In general, out-of-field dose from proton therapy is expected to be substantially lower than for photon therapy, particularly when using a pencil beam scanning method (Kry et al., 2017; Clasie et al., 2010).

2.5. Dosimetry

Radiation is detected using many different methods including radiochromic film, semiconductors, and thermoluminescent dosimeters. Each detection method has different benefits – some have excellent spatial resolution to accurately measure dose profiles for relative dosimetry, some are exceedingly sensitive to radiation exposure at the expense of accuracy, and many are optimized to measure absorbed dose using particular ranges of energies, dose rates, or radiation types.

2.5.1. Ionization chambers

An ionization chamber is a gas-filled chamber with a central electrode that collects charge. These chambers measure charge released in the chamber cavity by incident radiation; this charge is converted to dose via calibration to determine absorbed dose to the medium

surrounding the chamber. For high energy radiation where charged particle equilibrium cannot be assumed, this is often accomplished using Bragg Gray cavity theory (Task Group 21 et al., 1983).

When a gas-filled cavity is placed inside a medium, Bragg-Gray theory states that - under certain conditions - the ionization produced in the cavity is directly related to the absorbed dose to the surrounding medium (Bragg, 1912; Gray & Rutherford, 1936; Khan & Gibbons, 2014). The dose to the cavity is determined by the amount of charge generated in the cavity and the average energy absorbed per unit charge of ionization in the gas; the dose to the cavity is then related to the dose to the medium using the energy losses of electrons per path length ("stopping power") in the gas and the surrounding medium. The Spencer-Attix formulation of this theory instead uses the "restricted stopping power" to exclude dissipative electrons in the cavity (Spencer & Attix, 1955; Khan & Gibbons, 2014). Bragg-Gray cavity theory operates under certain conditions: the cavity must be small enough to not disturb the distribution of electrons throughout the medium, transient charged particle equilibrium must exist, and the charged particles collected in the cavity should be the result of radiation passing through the chamber (Khan & Gibbons, 2014).

Ionization chambers are often preferred for out-out-field photon measurements because of their low energy dependence (less than 4% for energies as low as 200 kV compared to Cobalt-60), particularly for chambers containing electrodes made of low atomic number materials (Kry et al., 2017; PTW, 2019). However, ion chambers are not always suitable for phantom measurements because of their size.

2.5.2. Thermoluminescent dosimeters

Thermoluminescent dosimeters (TLDs) use a crystalline chemical compound capable of capturing energy from incident radiation in the form of excited electrons. These electrons are trapped in an excited state within the crystal lattice and are subsequently released by exposing the material to thermal energy of a material-specific wavelength (Khan & Gibbons, 2014). The electrons transition back to a relaxed energy state and emit discrete photons of a known wavelength, which is then counted using a photon detector (typically a photomultiplier tube). The number of emitted photons during readout are proportional to the energy absorbed by the material, which can be calibrated to determine absorbed dose.

TLD use is well supported for out-of-field photon therapy measurements, with careful consideration of the TLD model's energy dependence, dynamic range, and nonlinear dose response. For example, LiF-based TLDs calibrated in the primary radiation field are known to overrespond to softer energy spectra seen out-of-field, resulting in overestimations up to 12% (Scarboro et al., 2011). In addition, some common TLDs (such as TLD-100s) are also known to overrespond to neutron radiation by factors of 10 or more, rendering them impractical for measuring out-of-field proton doses or photon radiations greater than 10 MV; however, other TLD types can be used for neutron measurements (Kry et al., 2017).

2.5.3. Diamond detectors

Synthetic single crystal diamond detectors uses a "Schottky diode" formed by the junction of a semiconducting material with a metal contact to capture charge carriers created by ionizing radiation, and generate a signal current that can be measured (PTW, 2016; Di Venanzio et al., 2013). The resulting signal can then be calibrated to determine absorbed dose. Synthetic

diamond detectors are typically used in situations requiring excellent spatial resolution, but also have desirable dosimetric characteristics for particle therapy. For example, studies have demonstrated that diamond detectors have very little dependence on LET for proton therapy (Rossomme et al., 2017), demonstrate good linearity with dose, and are independent on dose rate for scanning proton beams (Gomà et al., 2016).

2.6. Phantoms

Phantoms are constructs that facilitate measurements in radiation therapy, including quality assurance measurements and simulation of patient treatment. This study investigates the use of phantoms to simulate patient tissue.

In photon therapy, electron density is the most important aspect of tissue to emulate – since soft tissue and water have extremely similar electron densities, water is considered a suitable substitute for tissue for measurements. However, phantoms can be made with many types of materials, and are often composed of a plastic or epoxy resin that has a physical and electron density similar to water. Phantoms allow a dosimeter to be placed at the desired measurement location to approximate the dose absorbed in a patient. Ideally, this would be measured with an anthropomorphic phantom. However not all clinics have anthropomorphic phantoms, so they use solid water blocks for this purpose instead.

Solid water phantoms are commercially available, relatively inexpensive, and are easily assembled for measurements; for these reasons, any clinic undergoing regular quality assurance measurements will have solid water phantoms readily available. However, solid water phantoms are designed only to emulate the physical and electron densities of water, and the simple design of this phantom type indicates some necessary limitations in evaluating patient doses: they

cannot account for differing tissue types in the body (such as lungs and bones), and their rigid shapes cannot replicate a patient's body habitus.

Commercially produced anthropomorphic phantoms that emulate both external contour and tissue heterogeneities are available for use and are widely considered an excellent choice for measuring out-of-field doses. However, commercial anthropomorphic phantoms are not representative of individual patients since they cannot be personalized, and the financial burden of a whole-body phantom is prohibitive for many clinics. Additionally, the degree to which measurements are improved using an anthropomorphic phantom as compared to simpler, more readily available phantoms – if any – has not yet been determined.

3D-printing provides a potential solution for personalized, relatively inexpensive phantoms that can be used to conduct out-of-field dose measurement for specific patient treatments. For this reason, Louisiana State University developed and constructed a 3D-printed phantom prototype for out-of-field dose measurement research. This phantom was constructed using a light field image of an anthropomorphic phantom to 3D-print a PLA shell replicating its body habitus. The shell was printed in multiple sections, outfitted with a polyvinyl chloride (PVC) pipe in the longitudinal axis to allow dosimeter placement, and assembled to create a water-tight seal. The phantom was then filled with water for dose measurements to approximate the general radiation attenuation properties of soft tissue. This process is significantly less expensive than highly detailed commercial phantoms and can be personalized to allow measurements for high risk individual patients. These features, as well as the lightweight portability of the 3D-printed shell, make this phantom model a desirable option for out-of-field dose measurements.

The patient-specific phantom used in this study was 3D-printed to replicate a CIRS-706, a commercial anthropomorphic phantom (ATOM 10-year-old Model 706, CIRS, Inc., Norfolk,

Virginia). These phantoms model a 10-year-old female patient, and are shown in Figure 2. The accuracy of the 3D-printing assembly was evaluated by Carey et. al. and found to be in good agreement (Carey, 2019). The design of this 3D-printed phantom permits direct comparison of out-of-field dose measurement accuracy with an existing commercial phantom to validate its use for pediatric dose measurements.

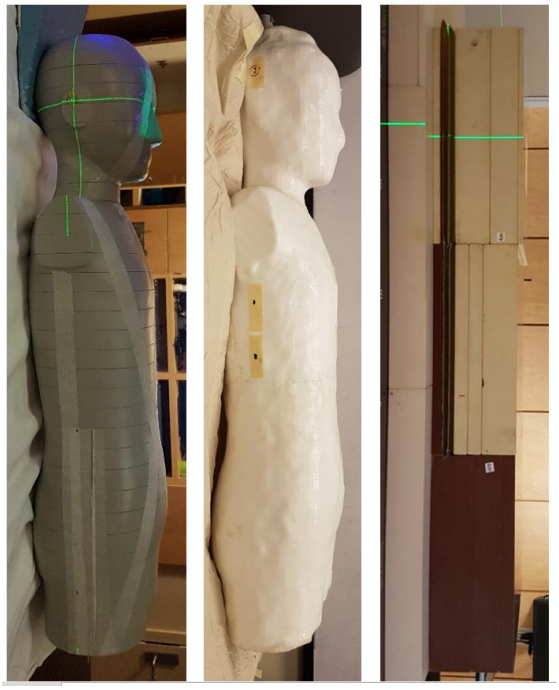

Figure 2: Photograph of the three phantoms used in this study: the CIRS-706 commerical phantom (left), Louisiana State University's 3D-printed phantom (center), and a solid water phantom (right).

3. Methods & Materials

3.1. Phantoms

Three phantoms were used to evaluate out-of-field photon dosimetry in this study, shown in Figure 2. The commercially available anthropomorphic phantom simulates a 10-year-old female

patient. CIRS Model 706 incorporates external contour and tissue heterogeneities and was used as the benchmark for validating photon out-of-field dose measurement in the 3D-printed phantom. CIRS Model 706 is manufactured in 2.5 cm thick axial slices, permitting the use of film measurements, and each slice is outfitted with removable plugs that can be replaced with small dosimeters. A CT image of an axial slice is shown in Figure 3.

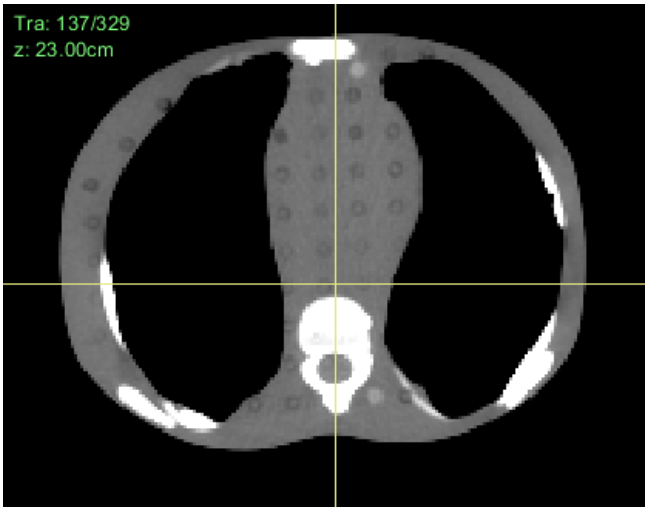

Figure 3: Transverse CT image showing interior heterogeneities, including lung tissue equivalent (black) and bone equivalent (white), in a pediatric commercial phantom (ATOM 10-year-old Model 706, CIRS, Inc., Norfolk, Virginia). The small, regularly spaced circles are removable plugs that can be replaced with dosimeters.

The 3D-printed phantom, developed and constructed at Louisiana State University, approximates the commercial phantom by replicating the external contour with a PLA shell. This PLA shell was printed using a light-field scan of CIRS Model 706, providing the basis for a direct comparison between the commercial and 3D-printed phantoms (Carey, 2019). The 3D-printed phantom was filled with water to simulate soft tissue, except for a 1.5 cm diameter PVC pipe fixed in the longitudinal axis at a depth of roughly 9 cm from the anterior surface. To better understand the importance of simulating tissue heterogeneities and the external contour of the patient, a third phantom was constructed using 30 x 30 cm^2 solid water blocks. The box

phantom was 90 cm long, 30 cm wide, and 17 cm deep, with an additional 0.7 cm slab placed at the superior end to better approximate the depth and SSD at isocenter, which coincides with the head of the phantom. Lateral views of the three phantoms are shown in Figure 2.

3.2. Photon out-of-field dosimetry

3.2.1. Measurement of out-of-field dose

A 6 megavoltage (MV) 10x10 cm^2 anterior-posterior intracranial photon field was delivered to each phantom at 100 cm SAD using a linear accelerator (Varian TrueBeam, Varian Medical Systems, Palo Alto, CA) at Oregon Health & Science University. Isocenter was defined at 8.75 cm depth, 7.4 cm inferior to the top of the CIRS and 3D-printed phantom head along the longitudinal axis. This location was chosen to permit measurement of an intracranial field between axial slices in the CIRS phantom and at the PVC pipe depth in the 3D-printed phantom.

Absorbed dose was measured using TLD-100 (LiF:Mg, Ti) powder capsules provided by IROC Houston (TLD-110, Imaging and Radiation Oncology Core, Houston, Texas). These dosimeters were chosen for their small uncertainty in measurement and relatively flat response to changes in energy spectrum introduced by out-of-field measurement compared to other dosimeters (Scarboro et al., 2011; Kry et al., 2007; Alvarez et al., 2017). In addition, their small size was necessary for out-of-field photon therapy measurements in the commercial anthropomorphic phantom, which could not accommodate an ion chamber. The TLD-100s were processed by IROC Houston's remote dosimetry audit system (Alvarez et al., 2017), and quality control chips were irradiated at IROC Houston on each day that measurements were taken to ensure accurate absorbed dose readings. All monitor units were scaled to deliver at least 30 cGy to the TLD-100s to minimize uncertainty, and results were normalized to 100 monitor units. For in-field

measurements, the uncertainty for linearity correction for the TLDs ranged from 0.3% to 1% for absolute doses from 25 cGy to 300 cGy (Alvarez, 2020). For out-of-field measurements, this uncertainty is expected to be less than 12% (Scarboro et al., 2011).

The four measurement locations chosen in this study corresponded to organs at risk of developing SMN in pediatric patients: thyroid, esophagus, small bowel, and gonads. Table 1 shows the depth and distance from the inferior edge of the intracranial field for each location.

Table 1: Out-of-field photon measurement locations with corresponding depths and distances from the nearest field edge.

Organ at Risk	Distance from 10x10 cm^2 intracranial field edge (cm)	Depth of measurement location in phantom (cm)		
		CIRS-706	3D-Printed	Solid Water
Thyroid	10.3	5.2	5.2	10
Esophagus	19.8	8.9	8.9	10
Small bowel	37.5	8.9	8.9	10
Gonads	55.1	8.8	8.8	10

Since the presence of the PVC pipe in the 3D-printed phantom dictated the allowable depth of each measurement, TLD depth in the CIRS phantom was replicated as closely as possible using registered CT scans of both phantoms. In the solid water phantom, the depth was fixed at 10 cm at all out-of-field locations. Since the dependence of out-of-field dose on depth is expected to be minimal (Stovall et al., 1995; Kry et al., 2017), these changes in measurement depth are not expected to contribute to changes in absorbed dose.

The TLD-100 placements in each phantom were secured to best suit the phantom design. In the commercial phantom, the TLD-100s were secured in small measurement slots created by removing plugs in the phantom's axial slices, as shown in Figure 3. In the solid water phantom, they were placed between two slabs of bolus. Finally, in the 3D-printed phantom they were placed within the PVC pipe embedded in a thin wooden dowel. These methods were chosen to secure the placement as accurately as possible and minimize potential air gaps.

At each measurement location, the out-of-field measured absorbed dose (D) per "prescription dose" (D_{Rx}) was compared between the three phantoms, in units of cGy/Gy. D/D_{Rx} measurements in the commercial phantom were considered the benchmark for all measurement locations.

3.2.2. TLD verification with ion chamber

To verify the accuracy of absorbed dose measurements in the TLD-100 capsules, ion chamber measurements were taken at each site-specific location using a PTW Farmer-type (0.6 cc active volume, air-filled) ionization chamber (Type 30013, PTW-Freiburg, Freiburg, Germany). Since the design of the commercial phantom does not permit ion chamber measurement without altering the phantom setup, this verification was performed in the solid water phantom only. Normalized absorbed dose per prescription dose measurements (cGy/Gy) were compared between the two detectors to ensure accurate TLD-100 measurements.

3.2.3. Sensitivity test

A sensitivity test was performed to assess the uncertainty introduced by small changes in distance from the field edge caused by erroneous detector placement. Since distance from the field edge is the primary influence in changes to out-of-field dose measurements, we considered that it is possible that small changes in detector placements may be more influential in contributing to dose differences between phantom measurements than the change of phantom itself.

A 6 MV 10x10 cm^2 field was administered using a linear accelerator (Varian TrueBeam), and the sensitivity test was performed in the solid water phantom at 10 cm depth using the calibrated 0.6 cc active volume farmer type ionization chamber. The solid water phantom was chosen to minimize variability in phantom depth and electron density.

Measurements were taken at each of the four locations corresponding to organs at risk (thyroid, esophagus, small bowel, and gonads), as well as at displacements 0.5, 1, 1.5, and 3 cm inferior and superior to each site-specific location. The larger displacement of 3 cm was chosen to estimate the possible displacement introduced by choosing a measurement location in a phantom to correspond to an individual patient's organ at risk, such as the thyroid.

3.3. Proton out-of-field dosimetry

Due to the novel coronavirus (COVID-19) pandemic, new proton therapy measurements following the methods outlined for the photon out-of-field dosimetry could not be acquired for this project. Instead, the methods for evaluating the 3D-printed phantom for proton out-of-field dosimetry were modified to include the processing and analysis of previous proton measurements taken in the 3D-printed phantom.

Measurements were planned and collected by Hunter Tillery, Margaret Carey, Dominic Maes, Erick Leuro, Philip Taddei, and Kyle Gallagher and other collaborators at the Seattle Care Cancer Alliance Proton Therapy Center (SPTC) (Tillery, 2019). To evaluate measurements in the 3D-printed phantom, an analytical model from the literature was used to supplement the missing internal neutron contribution to dose calculation by the treatment planning system (Gallagher & Taddei, 2018). This combination of calculated dose was used as the benchmark value to compare the measurements in the 3D-printed phantom.

3.3.1. Measurement of out-of-field dose

To simulate clinical protocols, a unique pediatric posterior-anterior craniospinal irradiation (CSI) treatment plan was created for the CIRS-706 commercial phantom. CT simulation for this treatment plan was performed on the commercial phantom and the 3D-printed phantom at the SPTC, and the CT image set was exported into RayStation to construct and calculate dose for a pencil-beam scanning proton therapy CSI treatment with a nominal energy of 200 MeV and prescription of 1.8 Gy-Relative Biological Effectiveness (RBE) to the cranial and spinal planning treatment volumes. The plan consisted of three posterior-anterior fields centered at the cranium, upper spine, and lower spine. The cranial field alone was evaluated for proton dosimetry in the 3D-printed phantom due to limitations of the applicability of the analytical model. A sagittal image of the cranial field applied to the commercial phantom is shown in Figure 4.

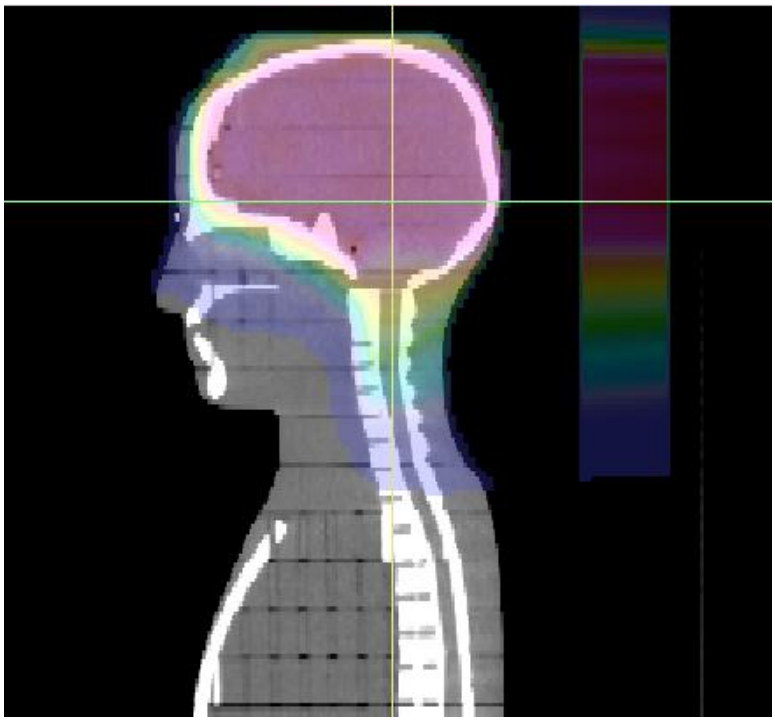

Figure 4: Planning image of cranial proton field used for a pediatric craniospinal irradiation treatment, as applied to a commercial phantom. Dose distribution is visualized as a color wash, where pink represents the prescription dose of 1.8 Gy-RBE. Image taken using CERR software (Deasy et al., 2003).

Out-of-field dose measurements were performed in the 3D-printed phantom using a 0.3 cc active volume tissue-equivalent ionization chamber (Wellhoffer IC-30, Ion Beam Applications, Louvain-La-Neuve, Belgium) filled with propane-based tissue-equivalent gas (5.039% Nitrogen, 41.00% Carbon dioxide, 53.961% Propane). A background measurement was collected over a 353 second time period. This value was scaled to 120 seconds (i.e. the beam-on time of the cranial field) and subtracted from each measurement. The IC-30 is primarily used for neutron dosimetry, and is applied to out-of-field proton dosimetry to measure absorbed dose from protons and neutrons in out-of-field proton dosimetry (Risler & Popescu, 2010; Moffitt et al., 2018; Tillery, 2019). The chamber was placed in the PVC pipe at locations corresponding to the

thyroid, esophagus, and gonads. Table 2 specifies the depth, distance from isocenter, and distance from the inferior edge of the clinical cranial field for each measurement location.

Table 2: Out-of-field proton measurement locations with corresponding depths and distances from the nearest field edge.

Organ at Risk	Distance from cranial isocenter (cm)	Distance from inferior field edge (cm)	Depth of measurement (cm)
Thyroid	12.6	4.1	5.2
Esophagus	22.8	16.7	8.9
Gonads	55.1	49.0	8.8

A microDiamond detector (Type 60019, PTW-Freiburg, Freiburg, Germany) was used to cross-calibrate absorbed dose measurements from the IC-30 and to measure the in-field absorbed dose at isocenter.

3.3.2. Calculation of out-of-field dose

Out-of-field dose for pencil beam scanning proton therapy is primarily composed of secondary neutrons, and more specifically, internal neutrons (Newhauser et al., 2009; Kry et al., 2017; Hälg & Schneider, 2020). The large radiation weighting factor for these neutrons make them a particularly concerning contribution to the out-of-field doses in proton therapy (ICRU, 1976). For these reasons, an analytical model that focuses on calculating equivalent dose deposition of

internal neutrons in pediatric intracranial proton therapy treatments was chosen for this study (Gallagher & Taddei, 2018).

Internal neutron calculations were carried out by applying the analytical model to the clinical cranial proton treatment field. This was done by exporting the simulated CIRS phantom and treatment plan as Digital Imaging and Communications in Medicine (DICOM) files. These files included the dose, plan, and structures of the dose calculation (RT dose, RT plan, and structure set), and a CT image of the phantom. The analytical model was applied using in-house codes, CERR (Deasy et al., 2003), and MATLAB® (Mathworks, MA, USA). In CERR, the 50% isodose line was constructed and exported to define the edge of the cranial field. The analytical model used this information to produce a distribution of internal neutron equivalent dose per prescription dose (H/D_{Rx} in mSv/Gy).

Because the internal neutron model calculated equivalent dose from internal neutrons (mSv/Gy), these values were converted to approximate the absorbed dose per prescription absorbed dose (mGy/Gy) by factoring out the average radiation weighting factor for neutrons applied over the algorithm, 7.86 (Newhauser et al., 2009). This value was then added to the out-of-field proton dose per prescription dose calculated by the RayStation treatment planning system (mGy/Gy) to represent the expected out-of-field absorbed dose at the thyroid, esophagus, and gonads.

The commercial phantom was chosen as the basis of calculation to provide the most accurate benchmark calculation for validation of the 3D-printed phantom. The analytical model implicitly accounted for tissue heterogeneities, whereas the treatment planning system explicitly accounted for heterogeneities in the commercial phantom for dose calculations.

4. Results

4.1. Photon out-of-field dosimetry

4.1.1. Measurement of out-of-field dose

Measured D/D_{Rx} (cGy/Gy) for photon therapy at all locations in the solid water, 3D-printed, and commercial phantoms are shown in Figure 5. For all measurements, D_{Rx} was defined as the dose at isocenter in the commercial phantom. D/D_{Rx} decreased with distance from the field edge and the out-of-field D/D_{Rx} measurements agreed well at each location across the three phantoms.

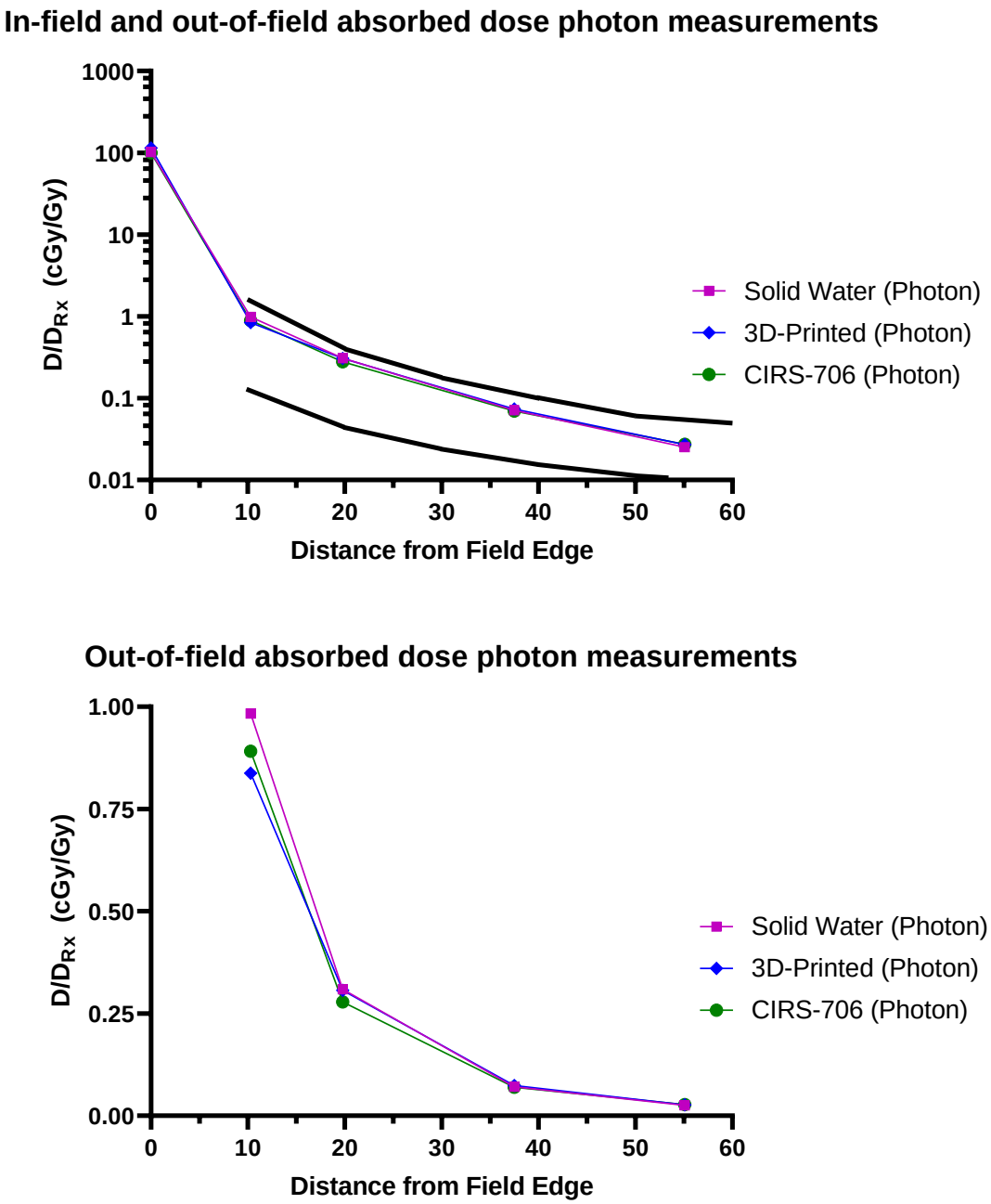

Figure 5: Out-of-field D/D_{Rx} in the solid water (purple squares), 3D-printed (blue diamonds), and CIRS phantoms (green circles). All measurements were conducted with TLD-100s and are reported in cGy/Gy. D_{Rx} is defined as the absorbed dose to isocenter in the CIRS phantom. The top image shows all measurements on a $\log_{10}$ scale, with upper and lower bounds (solid black lines) that estimate reasonably expected values for out-of-field photon dose

measurements as presented in the American Association of Physicists in Medicine's Task Group 158 (Kry et al., 2017). The bottom image shows the out-of-field measurements on a linear scale.

To further explore the differences in measurements between phantoms, the percent changes in D/D_{Rx} at each measurement location were calculated using the following equations, such that the expected value was the measurement in the phantom with more anthropomorphic detail:

$$\%\ Difference\ (SW, CIRS) = 100\% * \left(\frac{{}^{D}/_{D_{Rx}}(SW) - {}^{D}/_{D_{Rx}}(CIRS)}{{}^{D}/_{D_{Rx}}(CIRS)}\right); \quad \textit{Equation 1}$$

$$\%\ Difference\ (3D, CIRS) = 100\% * \left(\frac{{}^{D}/_{D_{Rx}}(3D) - {}^{D}/_{D_{Rx}}(CIRS)}{{}^{D}/_{D_{Rx}}(CIRS)}\right); \quad \textit{Equation 2}$$

$$\%\ Difference\ (SW, 3D) = 100\% * \left(\frac{{}^{D}/_{D_{Rx}}(SW) - {}^{D}/_{D_{Rx}}(3D)}{{}^{D}/_{D_{Rx}}(3D)}\right). \quad \textit{Equation 3}$$

These percent differences are plotted in Figure 6. These data demonstrate that the agreement between absorbed dose measurements between phantoms improved with increased distance from the field edge. We also observe that the largest difference in absorbed dose measurement with respect to the CIRS commercial phantom was at the esophagus, where D/D_{Rx} in the solid water phantom was 11.1% (0.031 cGy/Gy) larger.

Overall, the largest variation in D/D_{Rx} measurements across all phantoms was at the thyroid where D/D_{Rx} in the solid water phantom was 17.4% (0.146 cGy/Gy) larger than in the 3D-printed phantom. At the gonads the largest difference in D/D_{Rx} measurements was 7.7% (0.002 cGy/Gy), where the absolute difference in D/D_{Rx} measurements was negligible.

Figure 6 also shows that D/D_{Rx} measurement at the isocenter was up to 14.3% (14.3 cGy/Gy) larger in the 3D-printed phantom than in the other phantoms. It is important to note that despite attempts to minimize air gaps in the 3D-printed phantom, the head of the phantom had an air gap at the isocenter approximately 1.5 cm deep caused by incomplete filling of the 3D-

phantom shell at the nose. Otherwise, minimal air gaps were observed throughout the phantom.

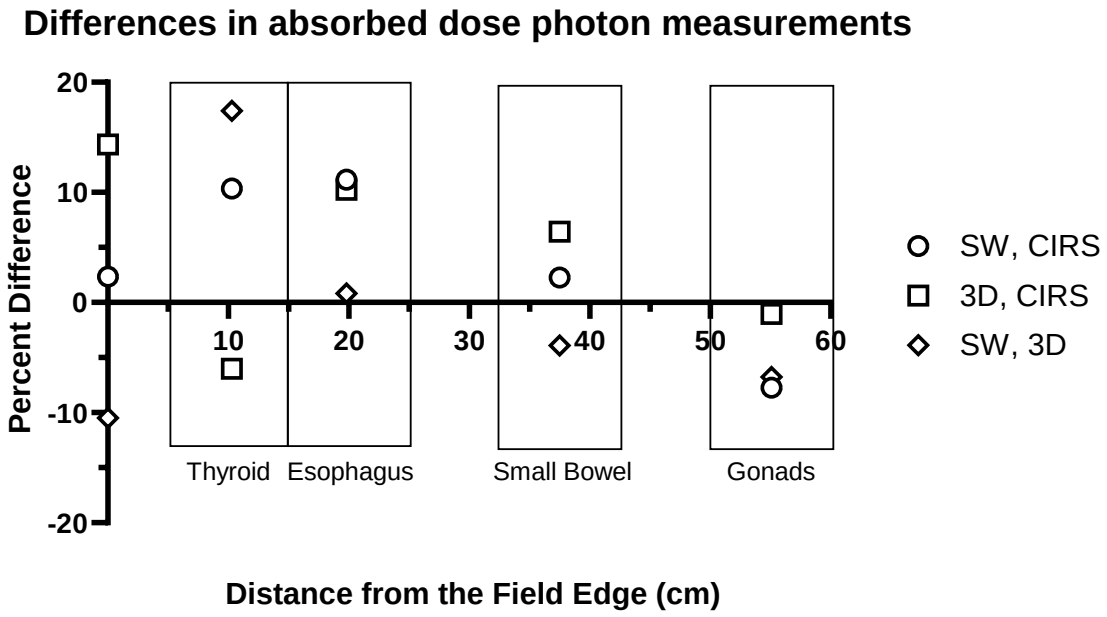

Figure 6: Percent differences in out-of-field D/D_{Rx} photon therapy measurements between phantoms versus distance from the field edge for each measurement location (thyroid, esophagus, small bowel, and gonads). Circles show percent differences in measurements between the solid water phantom and the CIRS phantom using Equation 1; squares show percent differences in measurements between the 3D-printed phantom and the CIRS phantom using Equation 2, and diamonds show percent differences in measurements between the solid water phantom and from the 3D-printed phantom using Equation 3. All measurements were conducted with TLD-100s and are reported in cGy/Gy.

4.1.2. TLD verification with ion chamber

Absorbed dose reported from TLD-100 readout was compared to ion chamber measurements. Table 3 summarizes measurements taken at all out-of-field locations in the solid water phantom using both TLD-100s and the farmer type ion chamber, verifying that measurements between

detector types varied less than 10.1% for all locations. The ion chamber reported a slightly higher dose than the TLD-100s at the isocenter (2.3%), which is acceptable for an in-field dose measurement, but reported lower doses than the TLD at all out-of-field locations. These data also showed that the agreement between detectors diverged with increasing distance from the field edge.

Table 3: Comparison of absorbed doses to the solid water phantom using an ionization chamber and thermoluminescent dosimeter (TLD) for 100 monitor units.

Location	**Distance from field edge (cm)**	**Absorbed dose for 100 monitor units (cGy)**		**Percent difference (IC, TLD)**
		PTW IC	**TLD-100**	
Isocenter	0	78.14	76.35	2.3%
Thyroid	10.3	0.690	0.734	-6.0%
Esophagus	19.8	0.211	0.231	-8.5%
Small bowel	37.5	0.0495	0.0530	-6.6%
Gonads	55.1	0.0169	0.0188	-10.1%

4.1.3. Sensitivity test

The characterization of the relationship between absorbed dose and detector placement sensitivity using an ion chamber in solid water phantom is shown in Figure 7. These data highlight how changes in absolute absorbed dose varied with small changes in detector placement close to and far from the field edge (i.e. 7.3 cm and 58.1 cm from the field edge). Near the field edge D/D_{Rx} fell off more rapidly than far from the field edge: from 7.3 to 8.8 cm

away from the field edge the D/D_{Rx} decreased by 0.304 cGy/Gy, whereas from 56.6 to 58.1 cm D/D_{Rx} only decreased by 0.0003 cGy/Gy.

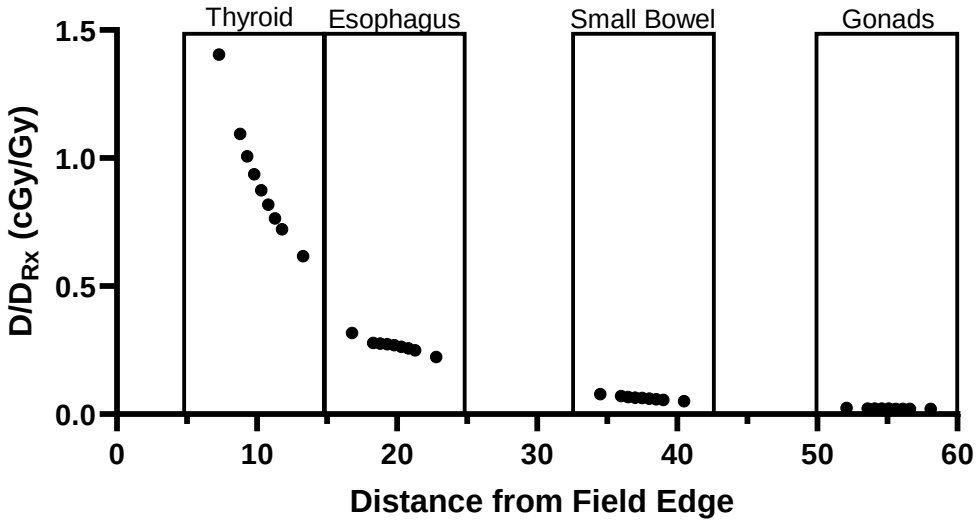

Figure 7: Out-of-field D/D_{RX} (cGy/Gy) for photon therapy versus distance from field edge, with error bars showing one standard deviation for each measurement location. Measurements are grouped in sections labeled with the site-specific measurement location of interest (thyroid, esophagus, small bowel, and gonads). All measurements were acquired using a PTW 30013 ion chamber in the solid water phantom.

The sensitivity of detector placement was also explored by observing differences in absorbed dose caused by offsets of 0.5, 1, 1.5 and 3 cm (closer to and further from the field edge) for each measurement location. The percent differences sorted by measurement location are shown in Figure 8, which demonstrate that near the field edge (at the thyroid) a shift in position as small as 1 cm resulted in changes in absorbed dose as large as 15.2% (0.13 cGy/Gy), and a shift of 3 cm resulted in changes as large as 60.6% (0.53 cGy/Gy). While this percent change decreases with distance from the field edge, these data show that even at distances greater than 55 cm from the field edge, an erroneous placement of a detector by a magnitude of 3 cm can still result in an overestimation of dose by 12.9% (0.003 cGy/Gy).

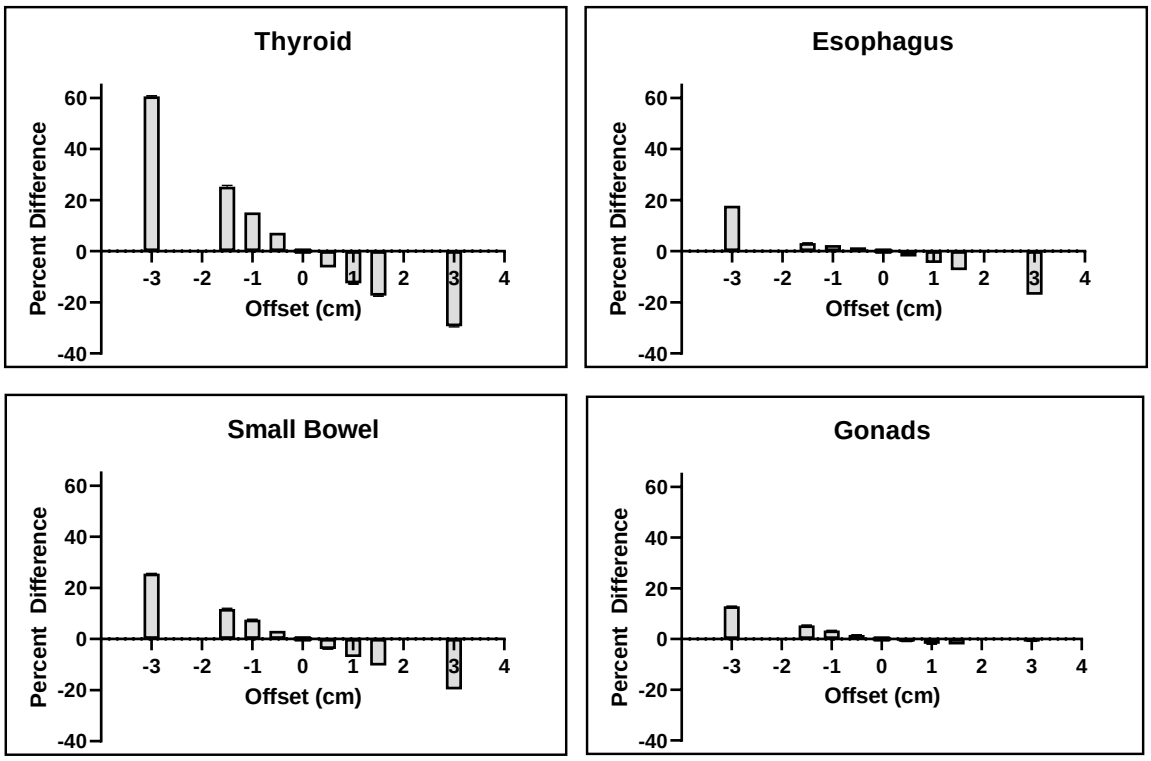

Figure 8: Percent differences in absorbed photon dose with respect to each organ at risk caused by detector placement offsets, with error bars showing one standard deviation for each measurement location. Negative offsets represent measurements closer to the field edge, and positive offsets are further away.

4.2. Proton out-of-field dosimetry

4.2.1. Measurement of out-of-field dose

Measurements of out-of-field D/D_{Rx} from proton therapy are shown in Figure 9 alongside the photon out-of-field D/D_{Rx} measurements, in units of cGy/Gy. For proton measurements D_{Rx} is defined as the dose to isocenter in the 3D-printed phantom.

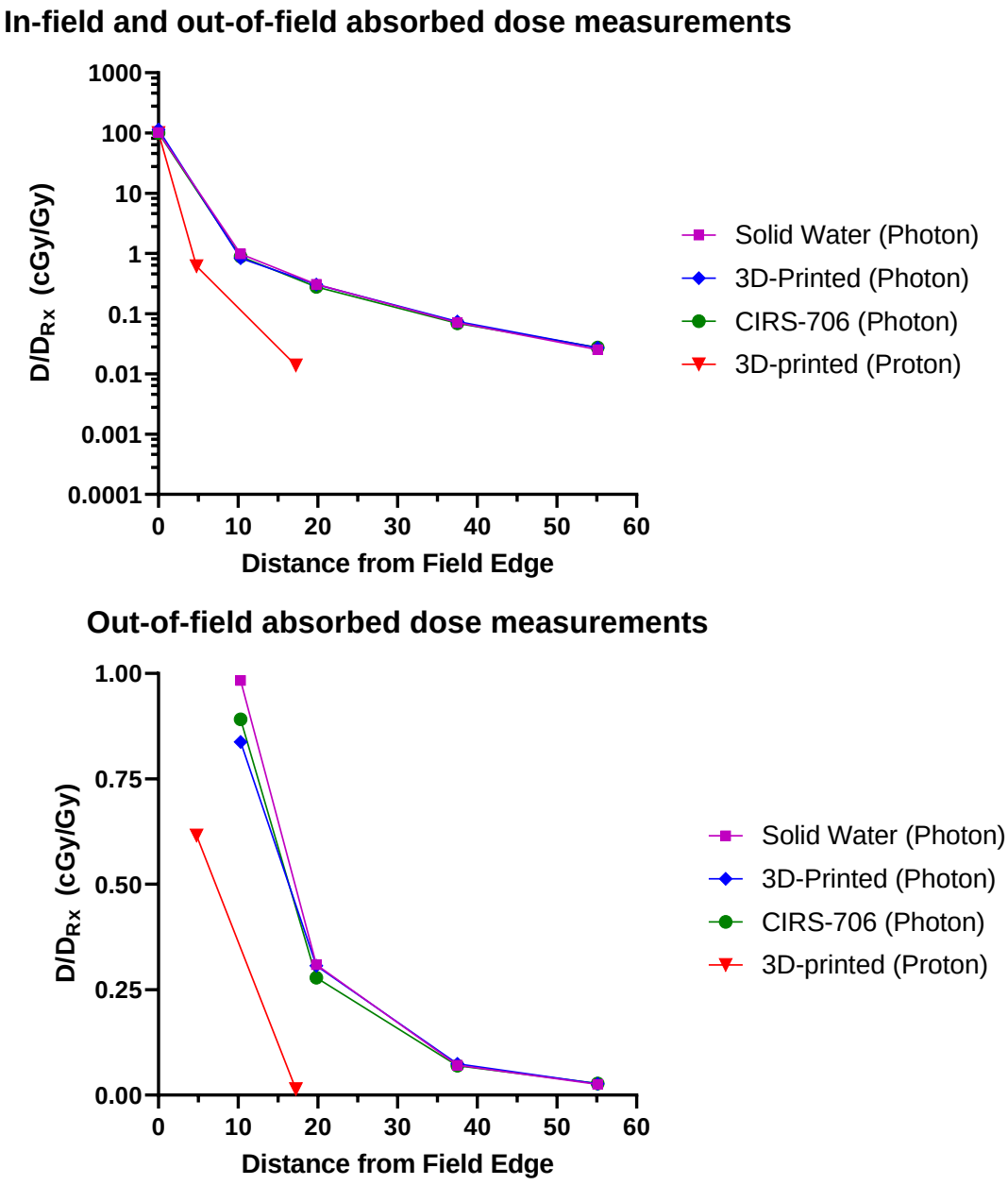

Figure 9: D/D_{Rx} measurements (cGy/Gy) from photon and proton therapy versus distance from the field edge. D/D_{Rx} for a cranial pencil-beam scanning proton field (red triangle) was measured in the 3D-printed phantom using an IC-30 chamber; measurements for a 10x10 cm^2 reference photon field were made in the solid water phantom (purple squares), 3D-printed (blue diamonds), and commercial phantoms (green circles) using TLD-100 capsules. Top: all measurements on a $\log_{10}$ scale. Bottom: out-of-field measurements on a linear scale. Gonad measurement for proton therapy was indistinguishable from background.

These data demonstrate that the measured D/D_{Rx} from proton therapy decreased with distance from the field edge, and that absorbed out-of-field dose from proton therapy was considerably lower than for photon therapy at each measurement location. Out-of-field dose at the gonads was indistinguishable from background for proton therapy. The lower proton D/D_{Rx} measurements were observed despite closer placement to the field edge for proton therapy measurements: because of differences in setup and beam arrangements between the cranial field used for proton therapy and the intracranial reference field used for photon therapy, each measurement location was between 2.5-5.5 cm closer to the nearest field edge for proton therapy than for photon therapy. For example, the thyroid measurement location was 4.1 cm from the field edge for proton therapy and 10.3 cm from the field edge in photon therapy.

4.2.2. Calculation of out-of-field dose

D/D_{Rx} measurements (mGy/Gy) for proton therapy were compared to the expected dose calculated using RayStation and an internal neutron analytical model in Figure 10. These data demonstrate that the calculated dose decreases substantially with distance from the field edge, in agreement with the absorbed dose measurements.

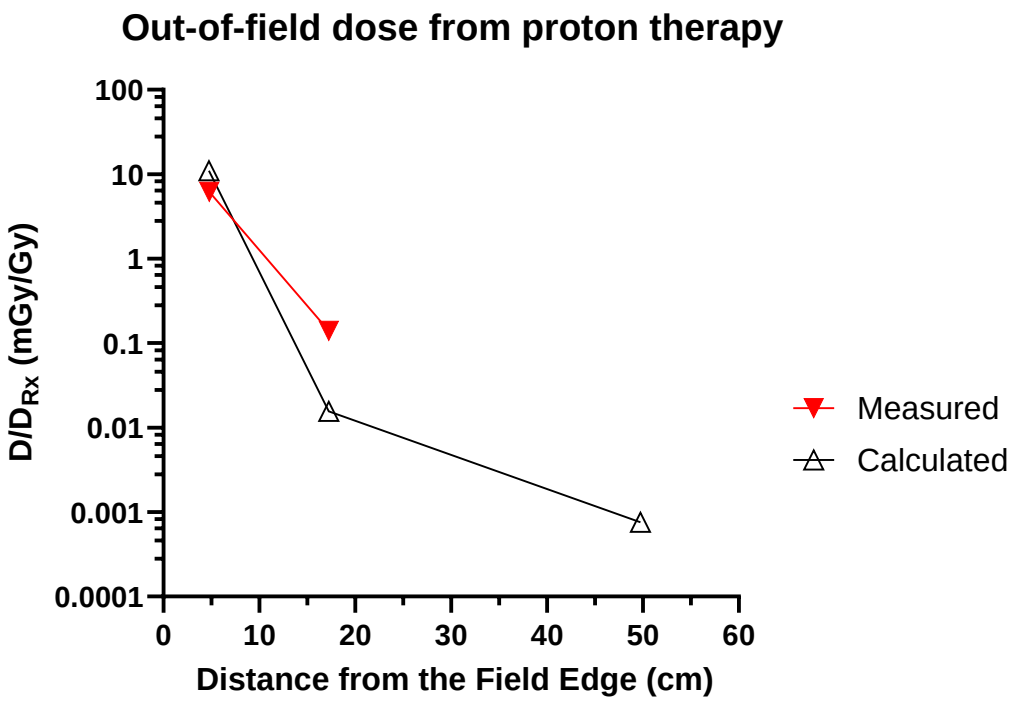

Figure 10: Measured out-of-field D/D_{Rx} using an IC-30 chamber (red) and calculated out-of-field D/D_{Rx} using proton dose from the RayStation treatment planning system and the internal neutron analytical model (black) are shown in units of mGy/Gy. Measured D/D_{Rx} at the gonads was intinguishable from background.

At the thyroid, the measured dose was 44% lower than the calculated dose, with an absolute difference of 4.85 mGy/Gy. At the esophagus, the measured dose was larger by 792% but the absolute difference in absorbed dose was 0.123 mGy/Gy. The calculated gonad dose was less than of the measured background dose, supporting the measured gonad dose's indistinguishability from background.

To test the sensitivity of the calculation model in high dose gradient regions, out-of-field dose was calculated using the treatment planning system and the analytical internal neutron model at locations 0.5 cm superior and inferior to the thyroid from a 1.8 Gy-RBE (i.e. 1.64 Gy) cranial proton treatment field. The results of these slight perturbations are shown in Table 4, which

demonstrate that at in high-gradient regions near the field edge a misplacement of 0.5 cm changed the calculated dose by up to 148 % (26.7 mGy).

Table 4: Changes in out-of-field absorbed dose from a 1.8 Gy-RBE (i.e. 1.64 Gy) proton cranial treatment field near the thyroid. The calculated out-of-field absorbed dose (mGy) at each position and the changes in calculated dose with respect to the calculated position are recorded. Changes are reported in absolute dose differences (mGy) and as a percent difference (%).

Distance from the field edge (cm)	**Calculated out-of-field absorbed dose (mGy)**	**Absolute (mGy) and percent (%) difference in calculated out-of-field absorbed dose to thyroid**
4.25	44.7	26.7 mGy (148%)
4.75	18.0	0 mGy (0%)
5.25	5.5	-12.5 mGy (-69%)

5. Discussion

5.1. Key Results

This study presented a preliminary validation of the use of a personalized pediatric 3D-printed anthropomorphic phantom for out-of-field photon dosimetry and an initial test was presented for use with out-of-field proton dosimetry. We also found that the differences in anthropomorphic phantom design had a minimal effect on the accuracy in out-of-field photon dosimetry between a CIRS commercial phantom, 3D-printed phantom, and solid water phantom.

Out-of-field D/D_{Rx} measurements showed good agreement between all three phantoms. For photon therapy, out-of-field D/D_{Rx} (cGy/Gy) measurements agreed within 17.4% between all three phantoms, and all D/D_{Rx} measurements in the 3D-printed phantom were within 11.1% of measurements in the commercial phantom at all of the out-of-field locations. The location with the largest disagreement between the 3D-printed and commercial phantom was at the esophagus, where the 3D-printed phantom reported a higher D/D_{Rx} than the commercial phantom. This location was very close to the lung, so the absence of lung-equivalent material in the 3D-printed phantom may have contributed to the larger measurement compared to the commercial phantom. TLD-100s have been found to overrespond to out-of-field dose from a 6 MV photon beams by as much as 12% (Scarboro et al., 2011), indicating that the differences in measurements between phantoms are on par with the uncertainty from TLD measurements. Additionally, the absolute differences in dose between phantoms were small, especially far from the field edge. These results demonstrate good agreement for 6 MV photon therapy across all three phantoms, especially between the 3D-printed phantom and the commercial phantom.

The sensitivity test demonstrated that out-of-field D/D_{Rx} measurements for photon therapy are highly sensitive to small displacements in dosimeter location relative to the field edge. These results suggest that differences in D/D_{Rx} measurements could have been influenced by variations in dosimeter placement, and further supports good agreement between measurements in all three phantoms. Furthermore, changes in out-of-field D/D_{Rx} influenced by shifts in detector position shown in Figure 8 suggest that the accuracy of detector position is more important than incorporating heterogeneities in the phantom for out-of-field measurements. This is particularly true for locations near the field edge.

For photon therapy, out-of-field D/D_{Rx} decreased with distance from the field edge, and the rate of dose falloff decreased as distance from the field edge increased. Examining data from the out-of-field photon dosimetry and the sensitivity test, the trends in out-of-field D/D_{Rx} measurements for photon therapy align well with experiments from the literature. The American Association for Physicists in Medicine Task Group 158 established a range of out-of-field D/D_{Rx} values that constitute "reasonably expected" out-of-field doses based on prior data, and our results fit within these bounds (Kry et al., 2017). Additionally, our results fit within an order of magnitude as a study that mapped out-of-field dose using ion chamber measurements in a solid water phantom for the same field on the same linear accelerator (Varian TrueBeam) (Wijesooriya, 2019). More specifically, D/D_{Rx} measurements taken using an ion chamber in our study agreed within 55% of theirs roughly 8 cm away from the field edge and within 25% approximately 15 cm from the field edge, where D/D_{Rx} measurements were taken at a depth of 2 cm in the literature. The results in this study show similar agreement with a study which evaluated out-of-field dose using TLD-100s in an acrylic phantom for the same reference field on a different linear accelerator (Varian Clinac 2100) (Kry et al., 2006). At approximately 10 cm from the field edge the D/D_{Rx} measurement using a TLD-100 in our study were within 45% those of

Kry et. al. at a depth of 2 cm in other settings. Our results were within a factor of 2 (126%, 1.1 cGy/Gy) of a feasibility study for a whole-body 3D-printed phantom using ion chamber measurements for a 10.3x10.3 cm^2 6 MV photon reference field on a different linear accelerator (Varian Novalis TX) (Tillery, 2019). Our results also agreed within approximately 40% near the field edge and within 0.02 cGy/Gy far from the field edge (i.e. the gonads) of D/D_{Rx} values calculated using an analytical model for out-of-field photon therapy (Gallagher et al., 2018). Overall, our data demonstrated good agreement with the literature despite different measurement locations, experimental setups, and dosimetric methods.

Proton therapy delivered substantially lower out-of-field D/D_{Rx} than photon therapy at the thyroid esophagus, and gonads, for which gonad measurement was indistinguishable from background. These results differed by approximately an order of magnitude from a study measuring out-of-field D/D_{Rx} from a 10.3x10.3 cm^2 intracranial proton field using an ion chamber filled with methane-based tissue equivalent gas in a personalized whole-body 3D-printed phantom (Tillery, 2019). Direct comparison between these measurements is difficult to discern because of differences in depth and distance from the field edge, different field sizes, and different phantom setups (Tillery, 2019). Similar agreements in out-of-field D/D_{Rx} measurements for proton therapy was found with data from the European Radiation Dosimetry Group Working Group 9, which measured out-of-field neutron dose from a lateral 10x10x10 cm^3 pencil beam scanning proton field with a nominal energy of approximately 170 MeV (with a nominal depth of 20 cm and a modulated depth of 10 cm) in a water phantom using a polyallyldiglycol carbonate-based track-etched dosimeter (Stolarczyk et al., 2018). The uncertainty associated with the track-etched dosimeters was estimated to be 30%, so agreement within an order of magnitude is acceptable given the differences in irradiated volume, nominal energy, and detector (Stolarczyk et al., 2018).

Finally, this study showed that the measured D/D_{Rx} from proton therapy was 44% smaller than the calculated dose at the thyroid, which is good agreement for out-of-field dose estimation. The measured D/D_{Rx} was 8 times larger at the esophagus compared to the calculated dose, which was a greater difference than expected. However, the absorbed dose to the esophagus was evaluated at a distance greater than 10 cm from the field edge, where doses are very small (< 50 mSv for a 23.4 Gy-RBE treatment) and the internal neutron model is known to have decreased accuracy (Gallagher & Taddei, 2018; Brenner et al., 2003). The good agreement at the thyroid constitutes a preliminary validation of the 3D-printed phantom for use in out-of-field proton dosimetry, but further investigation with additional measurement locations is warranted.

This thesis provides a unique contribution to the literature by evaluating the use of a personalized, inexpensive 3D-printed phantom for out-of-field photon dosimetry via direct comparison to a commercially available anthropomorphic phantom under nearly identical experimental parameters. Furthermore, this study provided further insight on the potential benefits of using an anthropomorphic phantom for out-of-field dosimetry using a comparable solid water phantom and found that the use of a simple solid water phantom can produce comparably accurate out-of-field dose measurements. These direct comparisons using three phantoms that emulate a single anatomical model provided a straightforward validation method for out-of-field photon dosimetry that can be applied to further understand the importance of including heterogeneities in phantom design for out-of-field dosimetry. Additionally, this study showed good agreement between measured absorbed dose in the 3D-printed phantom and the calculated dose for proton therapy at the thyroid.

5.2. Limitations

The presence of air gaps in the 3D-printed phantom may have affected the accuracy of out-of-field measurements. The air gap present in the head of the 3D-printed phantom reduced the effective depth of the isocenter measurement, resulting in a larger absorbed dose measurement to the isocenter in comparison to the other two phantoms: for photon therapy, the 3D-printed phantom reported an isocenter dose 14% higher than the commercial phantom and 10% higher than the solid water phantom. While the impact of this air gap is not expected to affect out-of-field dose measurements far from the field edge, it is possible that it affected near-field dose measurements at the thyroid. In addition, because the TLD-100 capsules were small compared to the PVC pipe diameter there was a small air gap between the water-filled phantom and the dosimeter. The full impact of this air gap on out-of-field measurement could benefit from further investigation.

Further work should reduce air gaps in the 3D-printed phantom as much as possible. The air gap in the head of the phantom can be eliminated by drilling a small hole into the nose of the phantom shell to allow air to escape and completely fill the phantom with water. The air gap in the PVC pipe could benefit from the use of a capsule to hold the TLD-100s and minimize the amount of air near the dosimeter. A suggested design is shown in Figure 11; a 3D-printed two-sided capsule 10 cm long could firmly secure the TLD-100s while providing ample scattering material within the pipe.

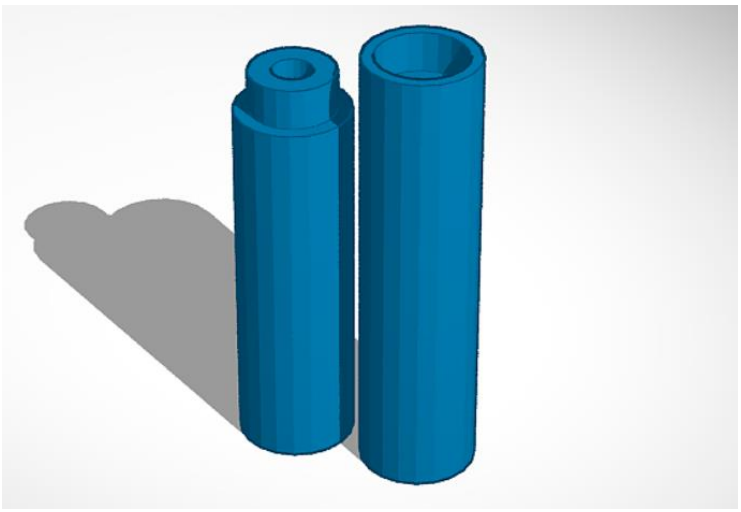

Figure 11: Proposed design for a 3D-printed capsule capable of securing TLD-100s and minimizing air gaps in the PVC pipe of the 3D-printed phantom developed at Louisiana State University.

The most unavoidable limitation of this study was the lack of measurements comparing out-of-field absorbed dose measurements for proton therapy in the 3D-printed phantom to the commercial and solid water phantoms; because of the COVID-19 pandemic, we were unable to obtain these measurements. This direct comparison of the accuracy of measurements in the 3D-printed phantom to the commercial phantom could be applied to validate its use for out-of-field proton dosimetry.

The uncertainty of proton therapy out-of-field measurements using the IC-30 in this study is not fully understood and requires further investigation. The propane-based tissue equivalent gas used in the IC-30 chamber for this study was different than the methane-based gas used in other studies (Moffitt et al., 2018; Tillery, 2019). This fill gas may have affected the response to incident radiation up to approximately 13%, and limits comparison to other studies (Moffitt, 2020). Furthermore, the use of a wooden dowel to position the dosimeter in the 3D-printed phantom may have introduced small errors in placement accuracy.

Calculation of out-of-field D/D_{Rx} for proton therapy using RayStation and the internal neutron analytical model has several limitations, including the omission of other potential out-of-field contributions. While internal neutrons were the dominant contributor (except for proton dose close to the field edge), the calculation method in this study did not account for external neutrons, photons, or other charged particles, whereas the IC-30 measured the absorbed dose from these contributions (Gallagher & Taddei, 2018).

Additionally, literature that has used the Monte Carlo dose engine in RayStation to evaluate proton doses near the field edge have observed that "for distances larger than 1 cm from the field edge RayStation tends to overestimate the dose" (Baumer et al., 2018). Our results may support this assessment, and the use of this treatment planning system for out-of-field proton determination requires further investigation.

Applying the internal neutron analytical model to calculate absorbed dose measurements from proton therapy in this study had the following limitations. First, the internal neutron model performs best at distances between 3 and 10 cm from the field edge, where doses are large enough to be of clinical relevance, and is not recommended beyond 20 cm (Gallagher & Taddei, 2018). This limitation indicates that the internal neutron dose calculations at the esophagus and gonads lack accuracy. Second, the analytical model was trained using intracranial fields that irradiated smaller volumes than the cranial field used in this study, so it may have underestimated the internal neutron dose (Gallagher & Taddei, 2018). Third, the model was trained to calculate equivalent doses using fields with nominal energies of 180 MeV, whereas the nominal energy of the measured field in this study was 200 MeV. Internal neutron dose is known to increase with increasing energy, therefore the model may have underestimated the equivalent dose in this study (Gallagher & Taddei, 2018). Third, the model is optimized to perform well for isolated intracranial fields, not for a cranial field for CSI like the one used in this

study. Cranial fields that are part of a CSI treatment have a shallow dose gradient to avoid unacceptable maximum and minimum doses at the junction of the cranial and spinal fields, which results in slower falloff and a 50% isodose surface that extends further inferiorly than a typical intracranial field. These features of the cranial field may have resulted in poorer performance of the analytical model (Gallagher & Taddei, 2018).

6. Summary & Conclusion

This study presents a preliminary validation for the use of a personalized 3D-printed phantom for out-of-field photon dosimetry via direct comparison to a commercially available anthropomorphic phantom and a solid water phantom under nearly identical experimental parameters. We found that the 3D-printed phantom was capable of facilitating accurate out-of-field dose measurements and that accuracy of dosimeter placement with respect to the field edge was of equal or greater importance than phantom design when measuring out-of-field dose, particularly at locations close to the field edge.

The findings of this study provide a preliminary test for using the 3D-printed phantom in proton out-of-field dosimetry. Out-of-field D/D_{Rx} for proton therapy was considerably lower than photon D/D_{Rx} at all measurement locations, and the out-of-field D/D_{Rx} measurement demonstrated good agreement with the calculated D/D_{Rx} at the thyroid. Out-of-field D/D_{Rx} measurements for proton therapy diverged from calculated D/D_{Rx} at locations further than 10 cm beyond the field edge, where the dose was low (i.e. less than 50 mSv). This study's use of direct comparisons of out-of-field dose measurements between three phantoms that emulate a single anatomical model provided a straightforward validation method for out-of-field photon dosimetry that can be applied to further validate the use of a 3D-printed phantom in out-of-field proton dosimetry.

This test of the 3D-printed phantom prototype has the potential for providing a personalized, cost-effective option for confirming out-of-field doses for pediatric patients who are at risk of developing secondary complications from out-of-field radiation exposure. Additionally, out-of-field dose measurements in 3D-printed phantoms may be used to validate efficient computational methods of determining out-of-field dose.

7. Bibliography

Alvarez, P. (2020, January 13, 2020). [TLD question].

Alvarez, P., Kry, S. F., Stingo, F., & Followill, D. (2017). TLD and OSLD dosimetry systems for remote audits of radiotherapy external beam calibration. *Radiat Meas, 106*, 412-415. doi:10.1016/j.radmeas.2017.01.005

Armstrong, G. T., Stovall, M., & Robison, L. L. (2010). Long-term effects of radiation exposure among adult survivors of childhood cancer: results from the childhood cancer survivor study. *Radiat Res, 174*(6), 840-850. doi:10.1667/RR1903.1

Athar, B. S., & Paganetti, H. (2011). Comparison of second cancer risk due to out-of-field doses from 6-MV IMRT and proton therapy based on 6 pediatric patient treatment plans. *Radiother Oncol, 98*(1), 87-92. doi:10.1016/j.radonc.2010.11.003

Baumer, C., Janson, M., Timmermann, B., & Wulff, J. (2018). Collimated proton pencil-beam scanning for superficial targets: impact of the order of range shifter and aperture. *Phys Med Biol, 63*(8), 085020. doi:10.1088/1361-6560/aab79c

Berrington de Gonzalez, A., Gilbert, E., Curtis, R., Inskip, P., Kleinerman, R., Morton, L., . . . Little, M. P. (2013). Second solid cancers after radiation therapy: a systematic review of the epidemiologic studies of the radiation dose-response relationship. *Int J Radiat Oncol Biol Phys, 86*(2), 224-233. doi:10.1016/j.ijrobp.2012.09.001

Berrington de Gonzalez, A., Vikram, B., Buchsbaum, J. C., de Vathaire, F., Dorr, W., Hass-Kogan, D., . . . Kleinerman, R. A. (2017). A Clarion Call for Large-Scale Collaborative Studies of Pediatric Proton Therapy. *Int J Radiat Oncol Biol Phys, 98*(5), 980-981. doi:10.1016/j.ijrobp.2017.03.033

Bethe, H. (1930). Zur Theorie des Durchgangs schneller Korpuskularstrahlen durch Materie. *Annalen der Physik, 397*(3), 325-400. doi:10.1002/andp.19303970303

Bloch, F. (1933). Zur Bremsung rasch bewegter Teilchen beim Durchgang durch Materie. *Annalen der Physik, 408*(3), 285-320. doi:10.1002/andp.19334080303

Bragg, W. H. (1912). *Studies in radioactivity*. London: MacMillan.

Brenner, D. J., Curtis, R. E., Hall, E. J., & Ron, E. (2000). Second malignancies in prostate carcinoma patients after radiotherapy compared with surgery. *Cancer, 88*(2), 398-406. doi:10.1002/(sici)1097-0142(20000115)88:2<398::Aid-cncr22>3.0.Co;2-v

Brenner, D. J., Doll, R., Goodhead, D. T., Hall, E. J., Land, C. E., Little, J. B., . . . Zaider, M. (2003). Cancer risks attributable to low doses of ionizing radiation: assessing what we really know. *Proc Natl Acad Sci U S A., 100*(24), 13761-13766 doi:10.1073/pnas.2235592100

Carey, M. (2019). Effect of personalized phantom 3-D printing and bone inclusion on radiotherapy treatment planning.

Clasie, B., Wroe, A., Kooy, H., Depauw, N., Flanz, J., Paganetti, H., & Rosenfeld, A. (2010). Assessment of out-of-field absorbed dose and equivalent dose in proton fields. *Medical Physics, 37*(1), 311-321. doi:10.1118/1.3271390

Craft, D. F., & Howell, R. M. (2017). Preparation and fabrication of a full-scale, sagittal-sliced, 3D-printed, patient-specific radiotherapy phantom. *J Appl Clin Med Phys, 18*(5), 285-292. doi:10.1002/acm2.12162

Craft, D. F., Kry, S. F., Balter, P., Salehpour, M., Woodward, W., & Howell, R. M. (2018). Material matters: Analysis of density uncertainty in 3D printing and its consequences for radiation oncology. *Med Phys, 45*(4), 1614-1621. doi:10.1002/mp.12839

Deasy, J. O., Blanco, A. I., & Clark, V. H. (2003). CERR: a computational environment for radiotherapy research. *Med Phys, 30*(5), 979-985. doi:10.1118/1.1568978

Di Venanzio, C., Marinelli, M., Milani, E., Prestopino, G., Verona, C., Verona-Rinati, G., . . . Pimpinella, M. (2013). Characterization of a synthetic single crystal diamond Schottky

diode for radiotherapy electron beam dosimetry. *Med Phys, 40*(2), 021712. doi:10.1118/1.4774360

Diallo, I., Haddy, N., Adjadj, E., Samand, A., Quiniou, E., Chavaudra, J., . . . de Vathaire, F. (2009). Frequency distribution of second solid cancer locations in relation to the irradiated volume among 115 patients treated for childhood cancer. *Int J Radiat Oncol Biol Phys, 74*(3), 876-883. doi:10.1016/j.ijrobp.2009.01.040

Eley, J., Newhauser, W., Homann, K., Howell, R., Schneider, C., Durante, M., & Bert, C. (2015). Implementation of an analytical model for leakage neutron equivalent dose in a proton radiotherapy planning system. *Cancers (Basel), 7*(1), 427-438. doi:10.3390/cancers7010427

Gallagher, K. J., & Taddei, P. J. (2018). Analytical model to estimate equivalent dose from internal neutrons in proton therapy of children with intracranial tumors. *Radiation Protection Dosimetry, 183*(4), 460-468. doi:10.1093/rpd/ncy166

Gallagher, K. J., Tannous, J., Nabha, R., Feghali, J. A., Ayoub, Z., Jalbout, W., . . . Taddei, P. J. (2018). Supplemental computational phantoms to estimate out-of-field absorbed dose in photon radiotherapy. *Phys Med Biol, 63*(2), 025021. doi:10.1088/1361-6560/aa9838

Gomà, C., Marinelli, M., Safai, S., Verona-Rinati, G., & Würfel, J. (2016). The role of a microDiamond detector in the dosimetry of proton pencil beams. *Zeitschrift für Medizinische Physik, 26*(1), 88-94. doi:https://doi.org/10.1016/j.zemedi.2015.08.003

Gray, L. H., & Rutherford, E. (1936). An ionization method for the absolute measurement of γ-ray energy. *Proceedings of the Royal Society of London. Series A - Mathematical and Physical Sciences, 156*(889), 578-596. doi:doi:10.1098/rspa.1936.0169

Gupta, A. C., Shrestha, S., Owens, C. A., Smith, S. A., Qiao, Y., Weathers, R. E., . . . Howell, R. M. (2020). Development of an age-scalable 3D computational phantom in DICOM standard

for late effects studies of childhood cancer survivors. *Biomedical Physics & Engineering Express*. doi:10.1088/2057-1976/ab97a3

Hälg, R. A., & Schneider, U. (2020). Neutron dose and its measurement in proton therapy—current State of Knowledge. *The British Journal of Radiology, 93*(1107), 20190412. doi:10.1259/bjr.20190412

Hall, E. J., & Amato, J. (2019). *Radiobiology for the Radiologist* (Eighth ed.). Philadephia, PA: Wolters Kluwer.

Hall, E. J., & Wuu, C. S. (2003). Radiation-induced second cancers: the impact of 3D-CRT and IMRT. *Int J Radiat Oncol Biol Phys, 56*(1), 83-88. doi:10.1016/s0360-3016(03)00073-7

Howell, R. M., Scarboro, S. B., Kry, S. F., & Yaldo, D. Z. (2010). Accuracy of out-of-field dose calculations by a commercial treatment planning system. *Phys Med Biol, 55*(23), 6999-7008. doi:10.1088/0031-9155/55/23/S03

Howell, R. M., Smith, S. A., Weathers, R. E., Kry, S. F., & Stovall, M. (2019). Adaptations to a Generalized Radiation Dose Reconstruction Methodology for Use in Epidemiologic Studies: An Update from the MD Anderson Late Effect Group. *Radiat Res, 192*(2), 169-188. doi:10.1667/RR15201.1

ICRP. (2007). *The 2007 Recommendations of the International Commission on Radiological Protection. ICRP publication 103* (0146-6453 (Print)

0146-6453). Retrieved from

ICRU. (1976). *Determination of Absorbed Dose in a Patient Irradiated by Beams (ICRU Report 24)*. Retrieved from Bethesda, MD:

ICRU. (1993). *Stopping Powers and Ranges for Protons and Alpha Particles (ICRU Report 49)*. Retrieved from Bethesda, MD:

Kaderka, R., Schardt, D., Durante, M., Berger, T., Ramm, U., Licher, J., & La Tessa, C. (2012). Out-of-field dose measurements in a water phantom using different radiotherapy modalities. *Phys Med Biol, 57*(16), 5059-5074. doi:10.1088/0031-9155/57/16/5059

Kase, K. R., Svensson, G. K., Wolbarst, A. B., & Marks, M. A. (1983). Measurements of dose from secondary radiation outside a treatment field. *Int J Radiat Oncol Biol Phys, 9*(8), 1177-1183. doi:10.1016/0360-3016(83)90177-3

Khan, F. M., & Gibbons, J. P. (2014). *Khan's the Physics of Radiation Therapy*. Philadelphia, UNITED STATES: Wolters Kluwer.

Kry, S. F., Bednarz, B., Howell, R. M., Dauer, L., Followill, D., Klein, E., . . . George Xu, X. (2017). AAPM TG 158: Measurement and calculation of doses outside the treated volume from external-beam radiation therapy. *Med Phys, 44*(10), e391-e429. doi:10.1002/mp.12462

Kry, S. F., Price, M., Followill, D., Mourtada, F., & Salehpour, M. (2007). The use of LiF (TLD-100) as an out-of-field dosimeter. *J Appl Clin Med Phys, 8*, 169-175.

Kry, S. F., Titt, U., Ponisch, F., Followill, D., Vassiliev, O. N., White, R. A., . . . Salehpour, M. (2006). A Monte Carlo model for calculating out-of-field dose from a varian 6 MV beam. *Med Phys, 33*(11), 4405-4413. doi:10.1118/1.2360013

Lomax, A. J., Boehringer, T., Coray, A., Egger, E., Goitein, G., Grossmann, M., . . . Wisser, L. (2001). Intensity modulated proton therapy: A clinical example. *Medical Physics, 28*(3), 317-324. doi:10.1118/1.1350587

Miften, M., Mihailidis, D., Kry, S. F., Reft, C., Esquivel, C., Farr, J., . . . Wilkinson, J. (2019). Management of radiotherapy patients with implanted cardiac pacemakers and defibrillators: A Report of the AAPM TG-203(dagger). *Med Phys, 46*(12), e757-e788. doi:10.1002/mp.13838

Moffitt, G. B. (2020, May 22, 2020). [Energy dependence of porpane-based tissue-equivalent gas].

Moffitt, G. B., Stewart, R. D., Sandison, G. A., Goorley, J. T., Argento, D. C., Jevremovic, T., . . . Laramore, G. E. (2018). Dosimetric characteristics of the University of Washington Clinical Neutron Therapy System. *Phys Med Biol, 63*(10), 105008. doi:10.1088/1361-6560/aabd52

National Research Council. (2006). *Health risks from exposure to low levels of ionizing radiation: BEIR VII phase 2* (Vol. 7): National Academies Press.

NCRP. (1993). *NCRP Report 116, Limitation of Exposure to Ionizing Radiation*. Retrieved from Bethesda, MD:

Newhauser, W., & Durante, M. (2011). Assessing the risk of second malignancies after modern radiotherapy. *Nature, 11*, 438-448.

Newhauser, W., Koch, N., Hummel, S., Ziegler, M., & Titt, U. (2005). Monte Carlo simulations of a nozzle for the treatment of ocular tumours with high-energy proton beams. *Phys Med Biol, 50*(22), 5229-5249. doi:10.1088/0031-9155/50/22/002

Newhauser, W., Schneider, C. W., Wilson, L., Shrestha, S., & Donahue, W. (2017). A review of analytical models of stray radiation exposures from photon- and proton-beam radiotherapies. *Radiation Protection Dosimetry*. doi:10.1093/rpd/nc0000

Newhauser, W. D., Berrington de Gonzalez, A., Schulte, R., & Lee, C. (2016). A Review of Radiotherapy-Induced Late Effects Research after Advanced Technology Treatments. *Front Oncol, 6*, 13. doi:10.3389/fonc.2016.00013

Newhauser, W. D., Fontenot, J. D., Mahajan, A., Kornguth, D., Stovall, M., Zheng, Y., . . . Woo, S. (2009). The risk of developing a second cancer after receiving craniospinal proton irradiation. *Phys Med Biol, 54*(8), 2277-2291. doi:10.1088/0031-9155/54/8/002

Newhauser, W. D., Fontenot, J. D., Taddei, P. J., Mirkovic, D., Giebeler, A., Zhang, R., . . . Mohan, R. (2009). Contemporary Proton Therapy Systems Adequately Protect Patients from Exposure to Stray Radiation. *AIP Conf Proc, 1099*(1), 450-455. doi:10.1063/1.3120071

Newhauser, W. D., & Zhang, R. (2015). The physics of proton therapy. *Phys Med Biol, 60*(8), R155-209. doi:10.1088/0031-9155/60/8/R155

Oeffinger, K. C., Mertens, A. C., Sklar, C. A., Kawashima, T., Hudson, M. M., Meadows, A. T., . . . Robison, L. L. (2006). Chronic Health Conditions in Adult Survivors of Childhood Cancer. *New England Journal of Medicine, 355*(15), 1572-1582. doi:10.1056/NEJMsa060185

PTW. (2016). microDiamond Synthetic Diamond Detector for High-Precision Dosimetry In P.-T. Werkstätten (Ed.), *Detectors*. https://www.ptwdosimetry.com/en/products/microdiamond/.

PTW. (2019). Ionizing Radiation Detectors Including Codes of Practice. In P.-T. Werkstätten (Ed.). https://www.ptwdosimetry.com/fileadmin/user_upload/DETECTORS_Cat_en_16522900_12/blaetterkatalog/index.html#page_96.

Risler, R., & Popescu, A. (2010). Dosimetry measurements at the fast neutron therapy facility in Seattle. *Radiation Measurements, 45*(10), 1452-1454. doi:10.1016/j.radmeas.2010.08.017

Rooney, M. K., Rosenberg, D. M., Braunstein, S., Cunha, A., Damato, A. L., Ehler, E., . . . Golden, D. W. (2020). Three-dimensional printing in radiation oncology: A systematic review of the literature. *J Appl Clin Med Phys*. doi:10.1002/acm2.12907

Rossomme, S., Marinelli, M., Verona-Rinati, G., Romano, F., Cirrone, P. A. G., Kacperek, A., . . . Palmans, H. (2017). Response of synthetic diamond detectors in proton, carbon, and oxygen ion beams. *Med Phys, 44*(10), 5445-5449. doi:10.1002/mp.12473

Salloum, R., Chen, Y., Yasui, Y., Packer, R., Leisenring, W., Wells, E., . . . Armstrong, G. T. (2019). Late morbidity and mortality among medulloblastoma survivors diagnosed across three decades: a report from the childhood cancer survivor study. *Journal of Clinical Oncology*. doi:10.1200/JCO.18

Scarboro, S. B., Followill, D. S., Howell, R. M., & Kry, S. F. (2011). Variations in photon energy spectra of a 6 MV beam and their impact on TLD response. *Med Phys, 38*(5), 2619-2628. doi:10.1118/1.3575419

Schneider, C. W., Newhauser, W. D., Wilson, L. J., & Kapsch, R. P. (2019). A physics-based analytical model of absorbed dose from primary, leakage, and scattered photons from megavoltage radiotherapy with MLCs. *Phys Med Biol, 64*(18), 185017. doi:10.1088/1361-6560/ab303a

Shine, N. S., Paramu, R., Gopinath, M., Jaon Bos, R. C., & Jayadevan, P. M. (2019). Out-of-field dose calculation by a commercial treatment planning ststem and comparison by monte carlo simulation for varian TrueBeam. *Journal of Medical Physics, 44*(3), 156-175.

Siegel, R. L., Miller, K. D., & Jemal, A. (2019). Cancer statistics, 2019. *CA: A Cancer Journal for Clinicians, 69*(1), 7-34. doi:10.3322/caac.21551

Smith, M. A., Seibel, N. L., Altekruse, S. F., Ries, L. A., Melbert, D. L., O'Leary, M., . . . Reaman, G. H. (2010). Outcomes for children and adolescents with cancer: challenges for the twenty-first century. *J Clin Oncol, 28*(15), 2625-2634. doi:10.1200/JCO.2009.27.0421

Spencer, L. V., & Attix, F. H. (1955). A theory of cavity ionization. *Radiat Res., 3*(3), 239

Stokkevag, C. H., Schneider, U., Muren, L. P., & Newhauser, W. (2017). Radiation-induced cancer risk predictions in proton and heavy ion radiotherapy. *Phys Med, 42*, 259-262. doi:10.1016/j.ejmp.2017.04.022

Stolarczyk, L., Trinkl, S., Romero-Exposito, M., Mojzeszek, N., Ambrozova, I., Domingo, C., . . . Olko, P. (2018). Dose distribution of secondary radiation in a water phantom for a proton pencil beam-EURADOS WG9 intercomparison exercise. *Phys Med Biol, 63*(8), 085017. doi:10.1088/1361-6560/aab469

Stovall, M., Blackwell, C. R., Cundiff, J., Novack, D. H., Palta, J. R., Wagner, L. W., . . . Shalek, R. J. (1995). Fetal Dose from Radiotherapy with Photon Beams. *Medical Physics, 22*(1).

Taddei, P. J., Jalbout, W., Howell, R. M., Khater, N., Geara, F., Homann, K., & Newhauser, W. D. (2013). Analytical model for out-of-field dose in photon craniospinal irradiation. *Phys Med Biol, 58*(21), 7463-7479. doi:10.1088/0031-9155/58/21/7463

Taddei, P. J., Khater, N., Youssef, B., Howell, R. M., Jalbout, W., Zhang, R., . . . Newhauser, W. D. (2018). Low- and middle-income countries can reduce risks of subsequent neoplasms by referring pediatric craniospinal cases to centralized proton treatment centers. *Biomed Phys Eng Express, 4*(2). doi:10.1088/2057-1976/aaa1ce

Task Group 21, Radiation Therapy Committee, & American Association of Physicists in Medicine. (1983). A protocol for the determination of absorbed dose from high-energy photon and electron beams. *Med Phys, 10*.

Tillery, H. D. (2019). *Feasibility of out-of-field dosimetry in photon, proton, and neutron therapies using a 3D-printed patient-specific phantom.* (Master of Science). Oregon Health & Science University,

Wijesooriya, K. (2019). Part I: Out-of-field dose mapping for 6X and 6X-flattening-filter-free beams on the TrueBeam for extended distances. *Med Phys, 46*(2), 868-876. doi:10.1002/mp.13362

Wilson, L. J., Newhauser, W. D., Schneider, C. W., Kamp, F., Reiner, M., Martins, J. C., . . . Parodi, K. (2020). Method to quickly and accurately calculate absorbed dose from therapeutic

and stray photon exposures throughout the entire body in individual patients. *Med Phys*. doi:10.1002/mp.14018

Wilson, R. R. (1946). Radiological Use of Fast Protons. *Radiology, 47*(5), 487-491. doi:10.1148/47.5.487

Zacharatou Jarlskog, C., & Paganetti, H. (2008). Risk of developing second cancer from neutron dose in proton therapy as function of field characteristics, organ, and patient age. *Int J Radiat Oncol Biol Phys, 72*(1), 228-235. doi:10.1016/j.ijrobp.2008.04.069

Zanini, A., Durisi, E., Fasolo, F., Visca, L., Ongaro, C., Nastasi, U., . . . Annand, J. R. (2004). Neutron spectra in a tissue equivalent phantom during photon radiotherapy treatment by LINACS. *Radiat Prot Dosimetry, 110*(1-4), 157-160. doi:10.1093/rpd/nch205

Zheng, Y., Newhauser, W., Fontenot, J., Koch, N., & Mohan, R. (2007). Monte Carlo simulations of stray neutron radiation exposures in proton therapy. *Journal of Nuclear Materials, 361*(2), 289-297. doi:https://doi.org/10.1016/j.jnucmat.2006.12.016